Chapter 2

Theoretical foundation and review of SPP based optical waveguide devices

Contents

2.1 Introduction

Before discussing the proposed compact surface plasmonic optical waveguide device, a comprehensive survey on various optical devices is required to study the area of integrated optical processor. In this direction, this chapter provides theoretical background of integrated planar waveguide devices and previous works for elaboration of motivation of our works.

The organization of the rest of the chapter is as follows. Section 2.2 gives an idea of propagation of surface plasmon polariton (SPP) and discusses the dispersion relation of SPP in two-layer and multilayer systems. Section 2.3 provides a brief idea of the planar waveguide couplers- directional couplers (DC), multimode interference (MMI) couplers and two-mode interference (TMI) couplers. This section also gives a comparison of coupling characteristics of DC, TMI coupler and MMI coupler and justifies the reason of selection of TMI coupler as the basic device for this work. Section 2.4 gives a comprehensive survey on the SPP based MMI coupler structures, all-optical logic gates and tunable optical power splitters reported by previous researchers. As the transition region in the TMI coupler uses waveguide bends, section 2.4 also gives a brief idea of bent waveguides and the loss occurring in the waveguide bends. Because the optically controlled switching operation is obtained by application of optical pulse of KCl:Tl^0(1) laser in the nonlinear cladding, a brief overview of the KCl:Tl^0(1) color center lasers has been provided at the last part of section 2.4. The major issues to be addressed, derived from the survey of previous literature are discussed in section 2.5. The chapter is concluded in section 2.6.

2.2 Surface plasmon polariton

Plasmonics is a well-established and rapidly growing research field with a long history [4]. In the year 1902, R. W. Wood observed an anomalous decrease of intensity of light when reflected from a metallic grating [5]. The occurrence of this phenomenon can be related to the excitation of surface plasmonic waves due to the periodic structure of the metallic grating. Later in 1904, J. C. M. Garnett developed a theory of effective dielectric constant to explain the color of metallic glasses, known as the Maxwell-Garnett theory [14]. In the year 1908, G. Mie studied the scattering and absorption of light by spherical particles of arbitrary size [15]. These studies carried out in the beginning of the 20th century laid the

foundation of the research in the field of plasmonics.

The existence of surface plasmon polaritons (SPPs) was first predicted by R. H. Ritchie in the year 1957 [6] who studied SPP propagation in metallic films and derived the dispersion equations. Shortly thereafter, it was experimentally demonstrated in 1960 by C. J. Powell and J. B. Swan [7]. Study of excitation of surface plasmon polaritons by light in 1968 by A. Otto [16] and the study of SPPs in thin films by E. N. Economou in 1969 [17] were two remarkable milestones in the field of plasmonics. The topic started to gain attraction only in the 1980s when researchers realized the strong confinement of energy at the metal surface [8] and then the research in the field gradually gained momentum through the evolution of fabrication and characterization methods enabling studies of SPP at the nanometer dimensions [9].

2.2.1 Fundamentals of surface plasmon polariton

Surface plasmon polariton are electromagnetic surface waves which propagate at the interface separating a dielectric medium and a conducting medium [12]. These surface waves arise due to coupling of electromagnetic field to oscillations of free electrons in the metal surface and decay exponentially as one moves in a direction perpendicular to the interface [12]. Fig-2.1 shows the schematic

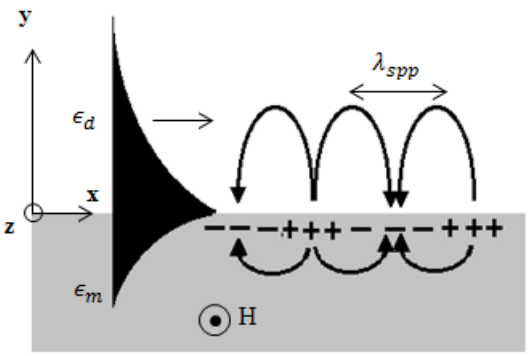

Figure 2.1: Schematic representation of propagation of SPP at metal-dielectric interface and the corresponding energy distribution

representation of propagation of surface plasmon polariton wave at the interface between a metal and a dielectric medium. The intensity distribution of the electromagnetic field components of the propagating SPP wave is also shown in Fig-2.1.

The physical properties of SPP wave can be analyzed with the help of the propagation constant of SPP propagation. As one of the two interacting media

consists of lossy material, the propagation constant of SPP wave is a complex quantity and can be expressed as

$$\beta = \beta_r + j\beta_{im} \tag{2.1}$$

where, β_r is the real part of propagation constant related to the effective refractive index of the medium and β_{im} is the imaginary part of propagation constant related to attenuation of the wave. The intensity of SPP wave decays exponentially along the direction of propagation. The intensity decays to 1/e times of its original value when the propagation distance is given by

$$L_P = \frac{1}{2\beta_{im}} \tag{2.2}$$

This value of propagation distance is known as the propagation length of SPP wave.

The propagation constant for surface plasmon polariton can be calculated with the help of the wave equation using proper boundary conditions. The wave equation can be written as follows [12]:

For TM polarization,

$$\begin{aligned} &\frac{\delta^2 H_y(z)}{\delta z^2} + \left(k_0^2\epsilon - \beta^2\right) H_y(z) = 0 \\ &E_x(z) = -j\frac{1}{\omega\epsilon_0\epsilon}\frac{\delta H_y(z)}{\delta z} \\ &E_z(z) = -\frac{\beta}{\omega\epsilon_0\epsilon}H_y(z) \end{aligned} \tag{2.3}$$

and for TE polarization,

$$\begin{aligned} &\frac{\delta^2 E_y(z)}{\delta z^2} + \left(k_0^2\epsilon - \beta^2\right) E_y(z) = 0 \\ &H_x(z) = -j\frac{1}{\omega\mu_0}\frac{\delta E_y(z)}{\delta z} \\ &H_z(z) = -\frac{\beta}{\omega\mu_0}E_y(z) \end{aligned} \tag{2.4}$$

where, $k_0 = 2\pi/\lambda$ and λ, ω, ϵ and ϵ_0 are the wavelength of operation, angular velocity of wave propagation, relative permittivity of the medium and permittivity of free space, respectively.

SPP dispersion relation for a single interface

Fig-2.2 shows the geometry for propagation of SPP at a single interface separating a metal with complex dielectric constant ϵ_m in the half space $z < 0$ and a dielectric with positive real dielectric constant ϵ_d in the half space $z > 0$. The

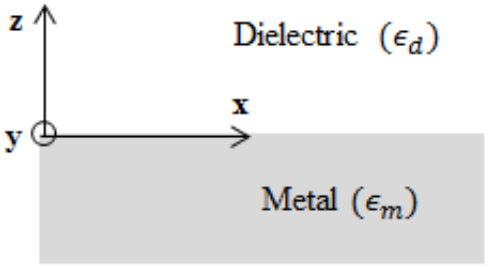

Figure 2.2: Geometry for propagation of surface plasmon polariton at metal-dielectric interface

solution of equation (2.3) for TM polarization can be written as follows:
For $z < 0$, in metal,

$$\begin{aligned} H_y(z) &= A_m \mathrm{e}^{j\beta x} \mathrm{e}^{k_m z} \\ E_x(z) &= -jA_m \frac{1}{\omega \epsilon_0 \epsilon_m} k_m \mathrm{e}^{j\beta x} \mathrm{e}^{k_m z} \\ E_z(z) &= -A_m \frac{\beta}{\omega \epsilon_0 \epsilon_m} \mathrm{e}^{j\beta x} \mathrm{e}^{k_m z} \end{aligned} \tag{2.5}$$

and for $z > 0$, in the dielectric medium,

$$\begin{aligned} H_y(z) =& A_d \mathrm{e}^{j\beta x} \mathrm{e}^{-k_d z} \\ E_x(z) =& jA_d \frac{1}{\omega \epsilon_0 \epsilon_d} k_m \mathrm{e}^{j\beta x} \mathrm{e}^{-k_d z} \\ E_z(z) =& -A_d \frac{\beta}{\omega \epsilon_0 \epsilon_d} \mathrm{e}^{j\beta x} \mathrm{e}^{-k_d z} \end{aligned} \tag{2.6}$$

where, A_m and A_d are constants. k_m and k_d are the components of wave vector in the two media, perpendicular to the interface, and can be written as

$$\begin{aligned} k_m^2 =& \beta^2 - k_0^2 \epsilon_m \\ k_d^2 =& \beta^2 - k_0^2 \epsilon_d \end{aligned} \tag{2.7}$$

Using the condition of continuity of $H_y(z)$ at the interface, equation (2.5) and (2.6) gives

$$A_m = A_d \tag{2.8}$$

Using the continuity of $E_x(z)$ at the interface, equation (2.5) and (2.6) gives

$$\frac{-A_m k_m}{\epsilon_m} = \frac{A_d k_d}{\epsilon_d} \tag{2.9}$$

Using equation (2.8) in (2.9), we get

$$\frac{-k_m}{\epsilon_m} = \frac{k_d}{\epsilon_d} \tag{2.10}$$

Using equation (2.7) in (2.10) and simplifying, we obtain

$$\begin{aligned} \beta^2 \left(\frac{1}{\epsilon_m^2} - \frac{1}{\epsilon_d^2}\right) &= k_0^2 \left(\frac{1}{\epsilon_m} - \frac{1}{\epsilon_d}\right) \\ \text{or} \qquad \beta^2 &= k_0^2 \left(\frac{\epsilon_m \epsilon_d}{\epsilon_m + \epsilon_d}\right) \\ \text{or} \qquad \beta &= k_0 \sqrt{\frac{\epsilon_m \epsilon_d}{\epsilon_m + \epsilon_d}} \end{aligned} \tag{2.11}$$

Equation (2.11) gives the dispersion relation for surface plasmon polariton wave propagating at the interface between the dielectric medium with dielectric constant ϵ_d and the conducting medium with dielectric constant ϵ_m and is valid for both the cases whether attenuation occurs (complex ϵ_m) or not (real ϵ_m).

However, surface plasmon polariton mode does not exist for TE polarization [12].

SPP dispersion relation for two parallel interfaces

In a multilayer system consisting of alternating films of dielectric and metal, bound SPP modes are present in each of the interfaces. Depending on the separation between the adjacent interfaces, SPP waves present in the interfaces interact and coupled SPP modes are generated.

The geometry of such a multilayer system is shown in Fig-2.3. The core layer with dielectric constant ϵ_1 and thickness $2a$ is sandwiched between two layers having dielectric constants ϵ_2 and ϵ_3, as shown in the figure. k_1, k_2 and k_3 are the components of wave vector in the corresponding medium, perpendicular

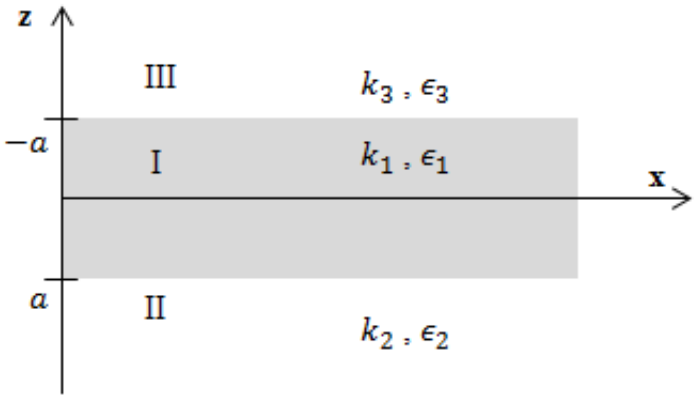

Figure 2.3: Geometry for propagation of SPP in a three-layer system

to the interfaces.

The solution of equation (2.3) for TM polarization in the three regions can be written as follows [12]:
For the region $z > a$ (layer III),

$$\begin{aligned} H_y(z) =& A\mathrm{e}^{j\beta x}\mathrm{e}^{-k_3 z} \\ E_x(z) =& jA\frac{1}{\omega\epsilon_0\epsilon_3}k_3\mathrm{e}^{j\beta x}\mathrm{e}^{-k_3 z} \\ E_z(z) =& -A\frac{\beta}{\omega\epsilon_0\epsilon_3}\mathrm{e}^{j\beta x}\mathrm{e}^{-k_3 z} \end{aligned} \tag{2.12}$$

For the region $z < -a$ (layer II),

$$\begin{aligned} H_y(z) =& B\mathrm{e}^{j\beta x}\mathrm{e}^{k_2 z} \\ E_x(z) =& -jB\frac{1}{\omega\epsilon_0\epsilon_2}k_2\mathrm{e}^{j\beta x}\mathrm{e}^{k_2 z} \\ E_z(z) =& -B\frac{\beta}{\omega\epsilon_0\epsilon_2}\mathrm{e}^{j\beta x}\mathrm{e}^{k_2 z} \end{aligned} \tag{2.13}$$

SPP wave in the core region results due to the coupling of the localized modes of the top and bottom interfaces. Thus, for $-a < z < a$ (layer I), we can write

$$\begin{aligned} H_y(z) =& C\mathrm{e}^{j\beta x}\mathrm{e}^{k_1 z} + D\mathrm{e}^{j\beta x}\mathrm{e}^{-k_1 z} \\ E_x(z) =& -jC\frac{1}{\omega\epsilon_0\epsilon_1}k_1\mathrm{e}^{j\beta x}\mathrm{e}^{k_1 z} + jD\frac{1}{\omega\epsilon_0\epsilon_1}k_1\mathrm{e}^{j\beta x}\mathrm{e}^{-k_1 z} \\ E_z(z) =& C\frac{\beta}{\omega\epsilon_0\epsilon_1}\mathrm{e}^{j\beta x}\mathrm{e}^{k_1 z} + D\frac{\beta}{\omega\epsilon_0\epsilon_1}\mathrm{e}^{j\beta x}\mathrm{e}^{-k_1 z} \end{aligned} \tag{2.14}$$

Here, A, B, C and D are constants and can be evaluated by applying the condition of continuity of $H_y(z)$ and $E_x(z)$ at the interfaces.

Applying the requirement of continuity of $H_y(z)$ and $E_x(z)$ at $z = a$, equations (2.12) and (2.14) gives

$$\begin{aligned} A\mathrm{e}^{-k_3 a} &= C\mathrm{e}^{k_1 a} + D\mathrm{e}^{-k_1 a} \\ \frac{A}{\epsilon_3} k_3 \mathrm{e}^{-k_3 a} &= -\frac{C}{\epsilon_1} k_1 \mathrm{e}^{k_1 a} + \frac{D}{\epsilon_1} k_1 \mathrm{e}^{-k_1 a} \end{aligned} \tag{2.15}$$

Applying the requirement of continuity of $H_y(z)$ and $E_x(z)$ at $z = -a$, equations (2.13) and (2.14) gives

$$\begin{aligned} B\mathrm{e}^{-k_2 a} &= C\mathrm{e}^{-k_1 a} + D\mathrm{e}^{k_1 a} \\ -\frac{B}{\epsilon_2} k_2 \mathrm{e}^{-k_2 a} &= -\frac{C}{\epsilon_1} k_1 \mathrm{e}^{-k_1 a} + \frac{D}{\epsilon_1} k_1 \mathrm{e}^{k_1 a} \end{aligned} \tag{2.16}$$

Further, $H_y(z)$ must satisfy the wave equation for TM polarization, given in equation (2.3) which gives

$$k_i^2 = \beta^2 - k_0^2 \epsilon_i \quad , \qquad i = 1, 2, 3 \tag{2.17}$$

Solving the linear system of the four coupled equations given in (2.15) and (2.16) along with equation (2.17), we obtain

$$\mathrm{e}^{-4k_1 a} = \left(\frac{k_1/\epsilon_1 + k_2/\epsilon_2}{k_1/\epsilon_1 - k_2/\epsilon_2} \right) \left(\frac{k_1/\epsilon_1 + k_3/\epsilon_3}{k_1/\epsilon_1 - k_3/\epsilon_3} \right) \tag{2.18}$$

Equation(2.18) gives the dispersion equation for a multilayer system with different substrate and superstrate. For infinite thickness of core ($a \to \infty$), equation (2.18) reduces to equation (2.11) which represents uncoupled SPP modes at the respective interfaces [12].

For a special case where the substrate (layer II) and superstrate (layer III) consist of the same material, we have $\epsilon_2 = \epsilon_3$ and hence $k_2 = k_3$. Thus, the dispersion equation (2.18) can be written as

$$\mathrm{e}^{-4k_1 a} = \left(\frac{k_1/\epsilon_1 + k_2/\epsilon_2}{k_1/\epsilon_1 - k_2/\epsilon_2} \right)^2 \tag{2.19}$$

Above equation can be split into a pair of independent equations which can be

written as

$$\tanh k_1 a = -\frac{k_2 \epsilon_1}{k_1 \epsilon_2} \tag{2.20}$$

$$\tanh k_1 a = -\frac{k_1 \epsilon_2}{k_2 \epsilon_1} \tag{2.21}$$

Equation (2.20) describes SPP modes having odd vector parity (function $E_x(z)$ is odd and functions $H_y(z)$ and $E_z(z)$ are even), whereas equation (2.21) describes SPP modes with even parity (function $E_x(z)$ is even and functions $H_y(z)$ and $E_z(z)$ are odd) [12].

2.2.2 Waveguiding of surface plasmon polaritons

Since the discovery of propagation of surface plasmonic modes, there have been several successful approaches to demonstrate confinement of surface plasmon polariton wave. There are innumerable ways to achieve waveguiding of SPP modes. A few of the most successful waveguide structures for SPP propagation, have been shown in Fig-2.4 [17–31] and discussed as follows:

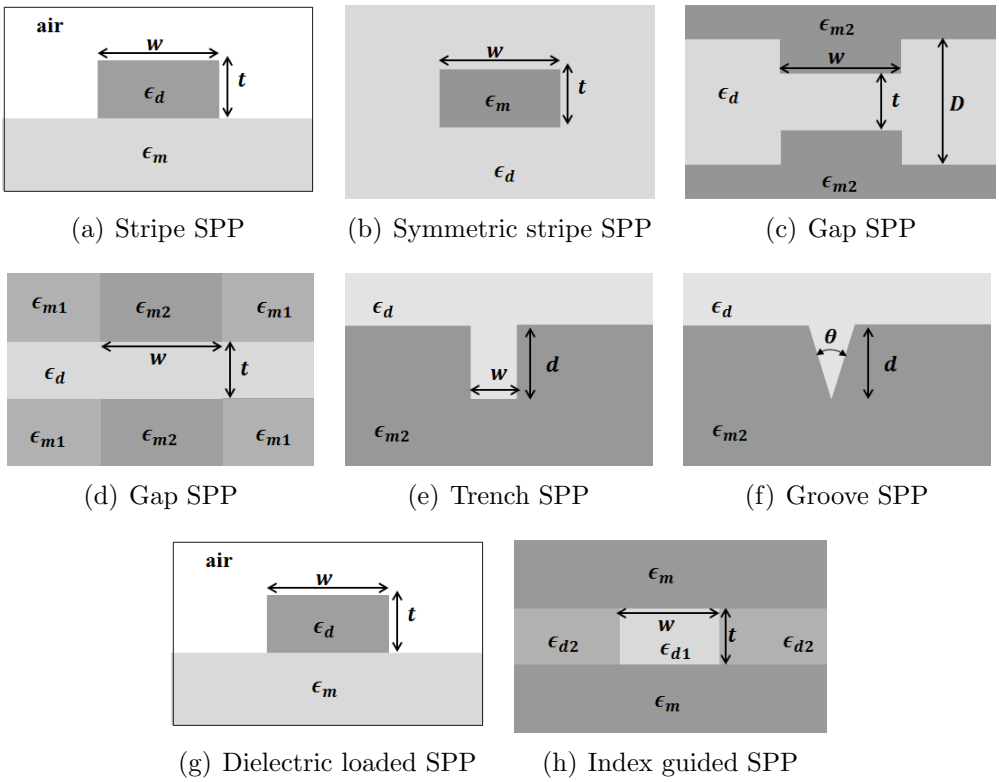

(a) Stripe SPP (b) Symmetric stripe SPP (c) Gap SPP

(d) Gap SPP (e) Trench SPP (f) Groove SPP

(g) Dielectric loaded SPP (h) Index guided SPP

Figure 2.4: Schematic geometry for a few waveguide structures for propagation of surface plasmon polaritons

1. **Stripe SPP waveguide**: The SPP waveguide configuration in which a metal stripe of finite width is placed on a dielectric substrate is known as stripe SPP waveguide (Fig-2.4(a)) [19,20]. This structure suffers from large radiation loss. For modes near cutoff, this radiation loss is even larger and exceeds the loss due to the absorption in metal [19].

2. **Symmetric stripe SPP waveguide**: Symmetric stripe SPP waveguide is a waveguide configuration in which a metal stripe of finite width is embedded in a dielectric substance (Fig-2.4(b)) [21, 22]. The propagation length of SPP modes in such a waveguide configuration is larger than the SPP modes in conventional waveguides. This length further increases as the stripe width decreases [18].

3. **Gap SPP waveguide**: Gap SPP waveguide structure consists of a symmetric metal-insulator-metal (MIM) configuration in which, a thin dielectric layer is sandwiched between two metal surfaces such that the metal extends infinitely on both sides of the dielectric [17,23,32,33]. Confinement of the gap SPP modes in the lateral direction can be achieved either by varying the gap width (shown in Fig-2.4(c)) [32] or by using two metals with different dielectric constants (as shown in 2.4(d)) [33].

4. **Channel SPP waveguide**: In channel SPP waveguides, guiding of SPP modes are achieved by a channel cut into a metal surface [24–27]. Such channels may either have a rectangular cross section (as shown in Fig-2.4(e)), also known as trench SPP waveguide [25–27], or a gradually varying cross section (as shown in Fig-2.4(f)) referred to as groove SPP waveguide [24, 25].

5. **Dielectric-loaded SPP (DLSPP) waveguide**: Dielectric loaded SPP (DLSPP) waveguide consists of a dielectric stripe of finite width placed on a metal surface (as shown in Fig-2.4(g)) [28, 29, 34]. Lateral confinement is achieved in such a waveguide structure, since the effective index of SPP modes supported by metal-dielectric interface is larger than that supported by metal-air interface [34]. The lateral confinement as well as mode propagation length can be improved by increasing the stripe thickness appropriately [28].

6. **Index guided SPP waveguide**: An index guided SPP waveguide is an MIM configuration in which the core dielectric layer consists of two

dielectrics, as shown in Fig-2.4(h). The dielectric with higher refractive index is the core, whereas the other dielectric is the side cladding [30, 31].

2.3 Planar waveguide couplers

The basic components of integrated optical devices are directional coupler (DC), multimode interference (MMI) coupler and two-mode interference (TMI) coupler. In this section, we discuss all these components and their working principles.

2.3.1 Directional Coupler (DC)

An optical directional coupler is a four port device which works on the principle that the field of the guided wave traveling in the core of the waveguide extends to the cladding, decaying exponentially as one moves away from the core-cladding interface [35]. Thus, when two waveguides are placed close to each other, separated by a very small gap (of the order of several wavelengths), transfer of optical power from one waveguide to the other takes place [36]. Fig-2.5 shows the three

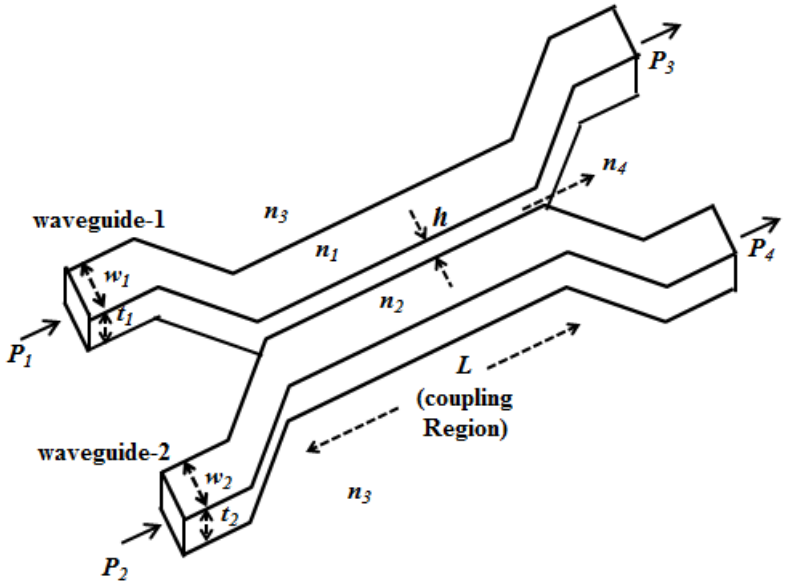

Figure 2.5: 3D schematic view of optical directional coupler

dimensional schematic view of an optical directional coupler. It consists of two rectangular waveguides separated by gap h in the coupling region. Width and thickness of waveguide-1 are w_1 and t_1 respectively, whereas width and thickness of waveguide-2 are w_2 and t_2 respectively. Refractive indices of the materials in core 1, core 2, the surrounding medium and the spacing between the two

waveguides are n_1, n_2, n_3 and n_4 respectively. β_1 and β_2 are the propagation constants of waveguide-1 and waveguide-2 respectively, without coupling. The coupling takes place in the region between $z = 0$ to $z = L$, in which even and odd modes can propagate with propagation constants β_e and β_o respectively. P_1 and P_2 are the input powers incident on waveguide-1 and waveguide-2 respectively whereas P_3 and P_4 are the output powers obtained at waveguide-1 and waveguide-2 respectively, after coupling.

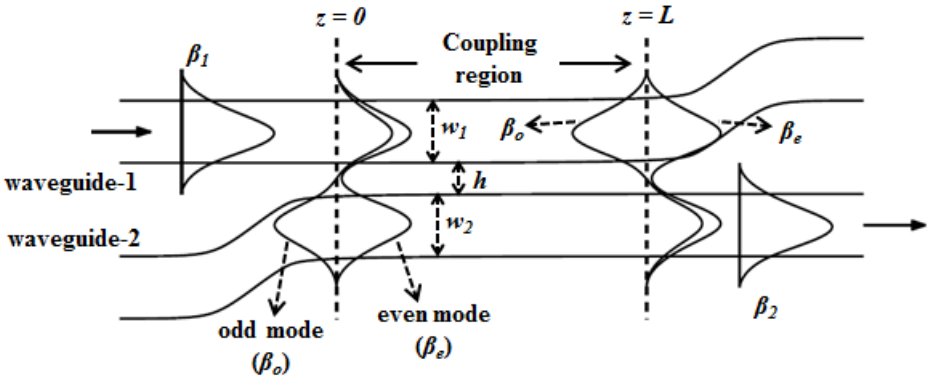

Figure 2.6: Operating principle of optical directional couplers

The operating principle of the optical directional coupler is illustrated in Fig-2.6. When a guided mode is incident on waveguide-1, the even and odd modes are excited at $z = 0$ in phase and with the same amplitude. As the two modes propagate, the phase difference increases. The propagation distance for which phase difference between the even and odd mode becomes π is called the coupling length and is written as [36]

$$L = \frac{\pi}{\beta_e - \beta_o} \tag{2.22}$$

The power transferred between the waveguides due to coupling of modes can be expressed in terms of the phase difference $(\beta_1 - \beta_2)$ between the guided modes in the two waveguides and the coupling coefficient κ which can be written as [36]

$$\kappa = \frac{1}{2}(\beta_e - \beta_o) \tag{2.23}$$

For a symmetrical directional coupler where $w_1 = w_2$, $t_1 = t_2$ and $n_1 = n_2$, i.e., $\beta_1 = \beta_2$, considerable coupling is observed when the separation between the waveguides is less than $8\mu m$ $(h < 8\mu m)$ [36]. Whereas, in an asymmetrical directional coupler where $w_1 \neq w_2$, and hence, $\beta_1 \neq \beta_2$, the separation must be less than $5\mu m$ $(h < 5\mu m)$ to observe coupling [36].

Coupled mode theory

The behavior of optical wave coupling in the waveguides can be successfully described with the help of coupled mode theory. The basic concept of coupled mode theory for two mode coupling is explained in the following paragraphs.

When the two waveguides-1 and 2 are close to each other, the guided modes propagating in the two waveguides interact through the evanescent field and there is a periodic exchange of energy between the two waveguides. This coupling can be explained with the help of the coupled mode equations. If $a(z)$ and $b(z)$ represents amplitude of a mode at z in waveguide-1 and waveguide-2 respectively and β_1 and β_2 are the propagation constants of waveguide-1 and waveguide-2 respectively, the coupled mode equations for the variation of amplitude of modes in the two waveguide can be written as [35]

$$\begin{aligned} \frac{da(z)}{dz} &= -j\beta_1 a(z) - j\kappa_{12} b(z) \\ \frac{db(z)}{dz} &= -j\beta_2 b(z) - j\kappa_{21} a(z) \end{aligned} \tag{2.24}$$

Here, κ_{12} and κ_{21} are constants referred to as coupling coefficients and represent the strength of coupling between the modes. The coupling coefficients are dependent on the waveguide parameters, gap between the waveguides in the coupling region and the operating wavelength. In the absence of coupling between the two modes, $\kappa_{12} = \kappa_{21} = 0$. For identical waveguides, $\kappa_{12} = \kappa_{21}$.

Power transferred due to coupling between waveguides

In order to solve the coupled mode equations, we have considered a wave in the system which is a superposition of the guided modes in the two waveguides and propagates with a phase constant β. Thus the amplitudes $a(z)$ and $b(z)$ can be written as

$$\begin{aligned} a(z) &= a_0 e^{-j\beta z} \\ b(z) &= b_0 e^{-j\beta z} \end{aligned} \tag{2.25}$$

where a_0 and b_0 are constants. Substituting $a(z)$ and $b(z)$ from equation (2.25) into equation (2.24), we get

$$\begin{aligned} a_0(\beta - \beta_1) &= \kappa_{12} b_0 \\ b_0(\beta - \beta_2) &= \kappa_{21} a_0 \end{aligned} \tag{2.26}$$

In order to get non-trivial solutions of equation (2.26), we must have

$$\beta^2 - \beta(\beta_1 + \beta_2) + \beta_1\beta_2 - \kappa^2 = 0 \tag{2.27}$$

where

$$\kappa = \sqrt{\kappa_{12}\kappa_{21}} \tag{2.28}$$

Thus,

$$\beta_{e,o} = \frac{1}{2}(\beta_1 + \beta_2) \pm \sqrt{\frac{1}{4}(\beta_1 - \beta_2)^2 + \kappa^2} \tag{2.29}$$

where the suffixes e and o indicate propagation constants for even and odd modes respectively which propagate in the coupling region.

Equation (2.29) can be written as

$$\beta_{e,o} = \beta_{av} \pm \sqrt{\delta\beta^2\kappa^2} \tag{2.30}$$

where, $\beta_{av} = (\beta_1 + \beta_2)/2$ and $\delta\beta = (\beta_1 - \beta_2)/2$. The general solution of the coupled mode equations can be written as

$$\begin{aligned} a(z) &= a_e e^{-j\beta_e z} + a_o e^{-j\beta_o z} \\ b(z) &= \frac{\beta_e - \beta_1}{\kappa_{12}} a_e e^{-j\beta_e z} + \frac{\beta_o - \beta_1}{\kappa_{12}} a_o e^{-j\beta_o z} \end{aligned} \tag{2.31}$$

where, a_e and a_o are constants denoting the amplitudes of the even and odd mode respectively and can be determined by using proper boundary conditions. Substituting equation (2.30) in equation (2.31), the solution of equation (2.24) can be written as

$$\begin{aligned} a(z) &= \left[a_e e^{-j\sqrt{\delta\beta^2+\kappa^2}z} + a_o e^{-j\sqrt{\delta\beta^2+\kappa^2}z}\right] e^{-j\beta_{av}z} \\ b(z) &= \left[\frac{\beta_e - \beta_1}{\kappa_{12}} a_e e^{-j\sqrt{\delta\beta^2+\kappa^2}z} + \frac{\beta_o - \beta_1}{\kappa_{12}} a_o e^{-j\sqrt{\delta\beta^2+\kappa^2}z}\right] e^{-j\beta_{av}z} \end{aligned} \tag{2.32}$$

We assume that, at $z = 0$, the guided mode is incident at waveguide-1 with unit power. We also assume that initially there was no power at waveguide-2 before the coupling takes place. Using appropriate boundary conditions, the output power at waveguide-1 and waveguide-2 at the end of coupling region i.e., at $z = L$ can be written as

$$\begin{aligned} \frac{P_3}{P_1} &= |a(z)|^2 = 1 - \frac{\kappa^2}{\kappa^2 + \delta\beta^2} \sin^2\left(\sqrt{\kappa^2 + \delta\beta^2} z\right) \\ \frac{P_4}{P_1} &= |b(z)|^2 = \frac{\kappa^2}{\kappa^2 + \delta\beta^2} \sin^2\left(\sqrt{\kappa^2 + \delta\beta^2} z\right) \end{aligned} \tag{2.33}$$

It can be seen from equation (2.33) that the power of the guided waves propagating in the two waveguides varies periodically. The minimum interaction length required for maximum power transfer is given by

$$L_\pi = \frac{\pi}{\sqrt{\kappa^2 + \delta\beta^2}} \tag{2.34}$$

The output power at waveguide-2 resulting from maximum coupling is written as

$$\begin{aligned} \frac{P_{4,max}}{P_1} &= \frac{\kappa^2}{\kappa^2 + \delta\beta^2} \\ &= \frac{1}{1 + \left(\frac{\delta\beta}{\kappa}\right)^2} \end{aligned} \tag{2.35}$$

In case of a symmetrical directional coupler, $\beta_1 = \beta_2$ and $\delta\beta = 0$. Thus the equation (2.33) can be written as

$$\begin{aligned} \frac{P_3}{P_1} &= \cos^2 \kappa z \\ \frac{P_4}{P_1} &= \sin^2 \kappa z \end{aligned} \tag{2.36}$$

Equation (2.36) gives the expressions for the output power obtained in the two waveguides at the end of the coupling region. The coupler is said to be in cross state when the entire power in waveguide-1 is transferred to waveguide-2. This is possible for z values given by $z = m\pi/\kappa, m = 0, 1, 2.....$ When the entire power in waveguide-1 remains in the same waveguide and no power is transferred to waveguide-2, the device is said to be in bar state. This occurs for z values given by $z = (m + 1/2)\,\pi/\kappa, m = 0, 1, 2.....$ The coupling length can be written as $L_\pi = \pi/2\kappa$. For strong interaction, the coupling coefficient is large and hence, the coupling length is small [37].

In case of an asymmetrical directional coupler where $\beta_1 \neq \beta_2$, there is an incomplete transfer of power between the waveguides [37]. The power transfer ratio is dependent on the factor $\delta\beta/\kappa$. The larger is $\delta\beta/\kappa$, the smaller is the power transfer ratio [37].

2.3.2 Multimode interference coupler (MMI)

Multimode interference coupler (MMI) is a waveguide device in which the central section is designed to support a large number of guided modes [38]. Depending

on the number of single mode input and output access waveguides used, the device is referred to as N×M MMI coupler where N is the number of input access waveguide used to launch light into the multimode section, whereas M is the number of output access waveguides used to recover light from the multimode section [38].

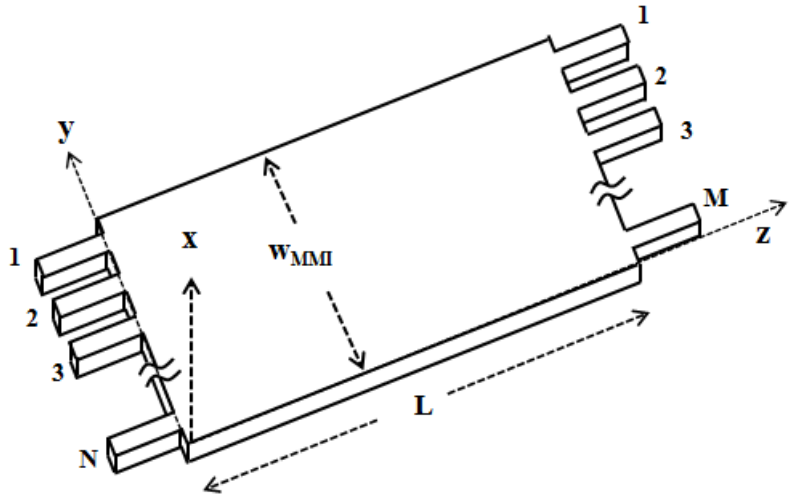

Figure 2.7: Three dimensional schematic view of a N×M MMI coupler

Fig-2.7 shows the three dimensional schematic view of an N×M MMI coupler. The width of the MMI section is w_{MMI} designed to support more than two modes whereas L is the length of the multimode region. On the other hand, the width of the N number of input access waveguides and the M number of output access waveguides is w, designed to support single mode. Refractive indices of the materials in the core and cladding are n_1 and n_2 respectively. The simplest MMI coupler is a 2×2 MMI coupler. The three dimensional schematic view of a 2×2 MMI coupler is shown in Fig-2.8, where two single mode waveguides are used as input access waveguides and two single mode waveguides are used as output access waveguides.

The principle of operation of optical MMI couplers can be explained with the help of self-imaging principle. Self-imaging can be defined as a property of multimode waveguides in which any input field incident on a multimode waveguide is reproduced at periodic intervals along the direction of propagation as single or multiple images. The phenomenon of self-imaging in multimode waveguides can be described by guided mode propagation analysis [38] as well as by other methods such as ray optics method [39], hybrid methods [40] etc.

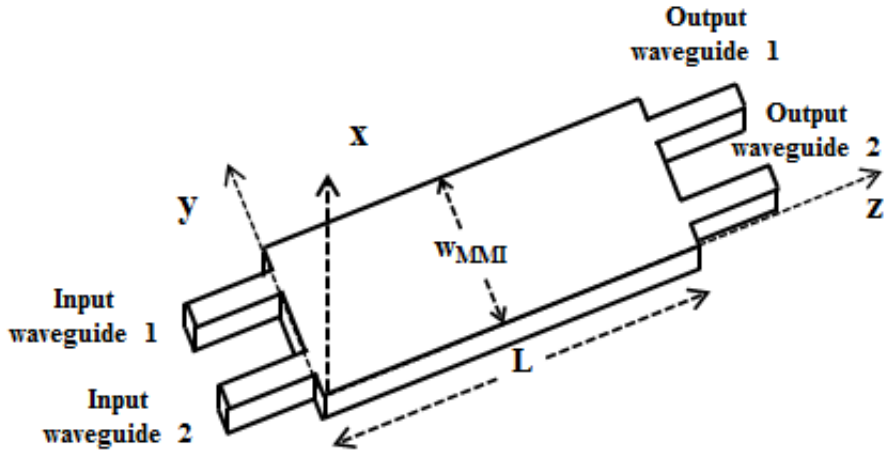

Figure 2.8: Three dimensional schematic view of a 2×2 MMI coupler

Guided mode propagation analysis

Guided mode propagation analysis is considered as an effective theoretical tool for the understanding of the phenomenon of self-imaging. It provides a basis for numerical modeling and design as well as explains the mechanism of multimode interference [38].

As the lateral dimension (along y-axis) in the multimode region is much larger compared to the transverse dimension (along x-axis), the waveguide can be expected to be single-moded in the transverse direction. Moreover, the same transverse behavior can be expected everywhere in the waveguide. Based on the above, the three dimensional waveguide can be replaced by a two dimensional waveguide (lateral and longitudinal) and the problem can be analyzed with the help of effective index methods. Fig-2.9 shows the two dimensional view of an

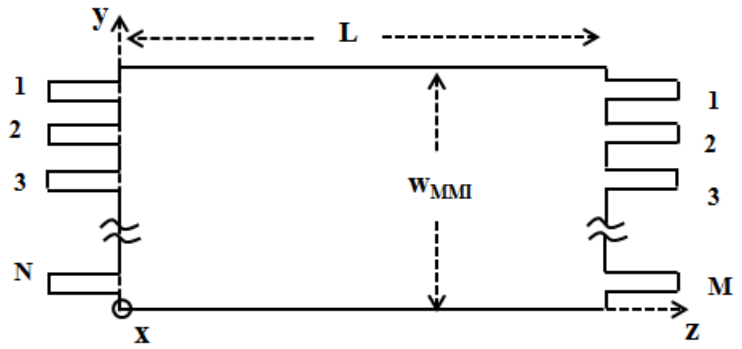

Figure 2.9: Two dimensional schematic view of a N×M MMI coupler

N×M MMI coupler shown in Fig-2.7.

The input field profile incident on the MMI waveguide at $z = 0$ is com-

posed of modal field distribution of all modes. For all practical applications, the spatial spectrum of the input field is so narrow that only guided modes are excited. In two dimensional approximations, input field profile $H(y,0)$ can be written as [38]

$$H(y,0) = \sum_{i=0}^{m-1} b_i H_i(y) \tag{2.37}$$

where, m is the total number of lateral modes supported and $H_i(y)$ is the mode field distribution of the ith mode. b_i is the mode field excitation coefficient of the ith mode and can be estimated by the analysis of sinusoidal modes [41]. For a 2×2 MMI coupler, b_i can be expressed as the Fourier series coefficient of periodic odd functions formed within the intervals from $-w$ to $+w$ and can be written as [42]

$$b_i = \frac{2}{w_{MMI}} \int_0^w sin\left(\frac{\pi y}{w}\right) sin\left[\pi(i+1)\frac{y}{w_{MMI}}\right] dy \tag{2.38}$$

The composite mode field profile at a distance z along the propagation direction, inside the MMI region can be expressed as the superposition of the mode field distribution of all the guided modes. This can be written as [38]

$$\begin{aligned} H(y,z) &= \sum_{i=0}^{m-1} H_i(y,z) \\ &= \sum_{i=0}^{m-1} b_i H_i(y) \exp[j(\beta_0 - \beta_i)z] \end{aligned} \tag{2.39}$$

where, β_i is the propagation constant of the ith mode. β_i is related to the core refractive index n_1, by the following equation [38]

$$\beta_i^2 = \left[\frac{2\pi}{\lambda} n_1\right]^2 - \left[\frac{(i+1)\pi}{W_e}\right]^2 \tag{2.40}$$

where, λ is the wavelength of operation. W_e is the effective width of the waveguide, taking into consideration the lateral penetration by each mode field. It can be written as

$$W_e = w_{MMI} + \left(\frac{\lambda}{\pi}\right)\left(\frac{n_2}{n_1}\right)^{2\sigma} \left(n_1^2 - n_2^2\right)^{-1/2} \tag{2.41}$$

where, $\sigma = 0$ for TE polarization and $\sigma = 1$ for TM polarization. Binomial expansion of equation (2.40) gives

$$\beta_i \simeq \frac{2\pi n_1}{\lambda} - \left[\frac{(i+1)^2 \pi \lambda}{4 n_1 W_e^2}\right] \tag{2.42}$$

Thus, the beat length for the two lowest order modes can be written as

$$L_\pi = \frac{\pi}{\beta_0 - \beta_1} \simeq \frac{4n_1 W_e^2}{3\lambda} \tag{2.43}$$

where, β_0 and β_1 are the propagation constants for the fundamental mode and first order mode respectively. Using equation (2.42) and (2.43), we can write,

$$\beta_0 - \beta_i \simeq \frac{i(i+2)\pi}{3L_\pi} \tag{2.44}$$

Substituting equation (2.44) into equation (2.39), the composite mode field profile at a distance $z = L$ along the propagation direction, at the end of the multimode region can be written as

$$H(y, L) = \sum_{i=0}^{m-1} b_i H_i(y) \exp\left[j\left(\frac{i(i+2)\pi}{3L_\pi}\right)L\right] \tag{2.45}$$

where, $(\beta_0 - \beta_i)L = [i(i+2)\pi/3L_\pi]L$ is the phase of the ith mode with respect to the fundamental mode at the end of the MMI region. The shape of the mode field $H(y, L)$ and the types of images hence formed depend on the mode field excitation coefficients b_i and the phase at the end of multimode region [38].

Depending on the mode excitation coefficient, the self imaging mechanism in MMI coupler can be of two types- general interference and restricted interference.

- General interference is the self-imaging mechanism in which the type of images formed is independent of the modal excitation. The number of images of input field formed along the multimode region is solely dependent on the phase factor $[i(i+2)\pi/3L_\pi]L$.

  In general interference, the output mode field will be a single image of the input field when $L = p(3L_\pi)$, $p = 0, 1, 2, 3....$ For even p, direct images are obtained and for odd p, the output is a mirror image of the input. N-fold images of input field will be formed for coupler length given by $L = p(3L_\pi)/N$, where $p \geq 0$ and $N \geq 1$ are integers with no common divisor.

- Restricted interference is the self-imaging mechanism in which only certain guided modes can be excited in the multimode region. Again, restricted interference can be of two types -paired interference and symmetric interference.

In case of paired interference, a three times reduction is observed in the length periodicity of the phase factor in equation (2.45) if $b_i = 0$ for $i = 2, 5, 8, ...$ etc. Thus, if the modes $i = 2, 5, 8, ...$ are not excited in the waveguide, single images will be obtained at $L = p(L_\pi)$. Also, N-fold images of the input field will be obtained at $L = p(L_\pi)/N$. Here, $p \geq 0$ and $N \geq 1$ are integers with no common divisor.

In case of symmetric interference, a four times reduction is observed in the length periodicity of the phase factor in equation (2.45) if $b_i = 0$ for odd integral values of i. Thus, if only the even modes are excited in the waveguide, single images will be obtained at $L = p(3L_\pi/4)$. Similarly, N-fold images of the input field will be obtained at $L = p(3L_\pi/4)/N$. Here, $p \geq 0$ and $N \geq 1$ are integers with no common divisor.

Power coupled to output waveguides

When optical power is incident on the input access waveguides, the power is either transferred to the output access waveguides or lost out by the time it reaches the end of the multimode region. The output access waveguides are designed so as to support only the fundamental mode. The mode field of the output access waveguides can be expressed as the collective contribution of all the guided modes propagating in the multimode region. For the Mth waveguide, the mode field profile can be written as

$$H_M(y, L) = \sum_{i=0}^{m-1} H_{M,i}(y, L) = \sum_{i=0}^{m-1} c_{M,i} H_i(y) \exp[j(\beta_0 - \beta_i)z] \tag{2.46}$$

where, $H_{M,i}(y, L)$ is the field contribution of ith mode to Mth output access waveguide and $c_{M,i}$ is the measure of contribution of ith mode to Mth output access waveguide which can be estimated by the analysis of sinusoidal modes [41]. For a 2×2 MMI coupler, $c_{M,i}$ can be expressed as the Fourier series coefficient of periodic odd functions formed within the intervals from $-w$ to $+w$ and can be written as

$$c_{M,i} = \frac{2}{w} \int_0^w \sin\left[\pi(i+1)\frac{y}{w_{MMI}}\right] \sin\left(\frac{\pi y}{w}\right) dy \tag{2.47}$$

The power obtained at the Mth output access waveguide is

$$P_M = |H_M(y, L)|^2 \tag{2.48}$$

2.3.3 Two-mode interference coupler (TMI)

Two-mode interference (TMI) coupler is a waveguide coupler in which the central section supports two guided modes- the fundamental mode and the first order mode. The schematic view of a TMI coupler is shown in Fig-2.10. It consists of a

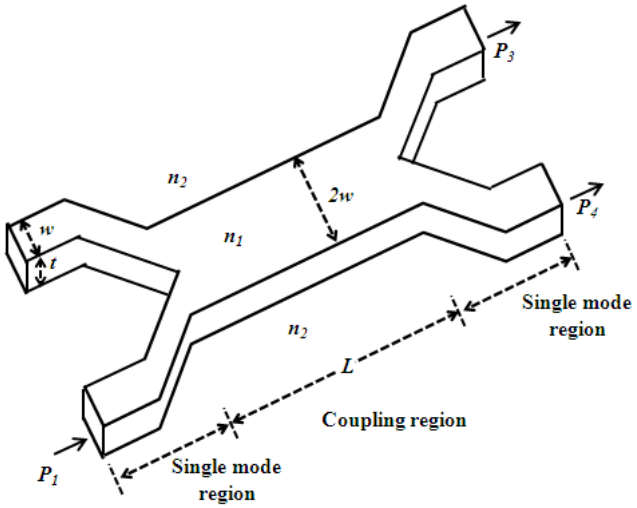

Figure 2.10: 3D schematic view of optical two-mode interference coupler

two-mode region of width $2w$, thickness t and length L and two single mode input access waveguides and two single mode output access waveguides with width w and same thickness t as that of the two-mode region. The refractive indices of the core and cladding are n_1 and n_2 respectively. Optical power P_1 is incident on the input access waveguide-1, whereas optical power P_3 and P_4 are obtained at the output access waveguides.

The principle of operation of TMI coupler can be explained by two-mode interference in the coupling region. When optical power is incident on the input access waveguides, the fundamental and first order modes are excited in the coupling region with different propagation constants β_{00} and β_{01} respectively [43, 44] and interfere with each other. Depending on the relative phase of these two guided modes at the end of the coupling region, optical power is coupled to the output access waveguides. The beat length of TMI coupler i.e., the minimum length of coupling region corresponding to π phase difference between the two guided modes can be written as

$$L_\pi = \frac{\pi}{\beta_{00} - \beta_{01}} \tag{2.49}$$

Power coupled to output waveguides

In a two-mode interference (TMI) coupler, the expression for the power transfer ratio can be obtained with an understanding of the coupled mode theory. Power transferred to the output access waveguides in a TMI coupler can be written as [44]

$$\begin{aligned} \frac{P_3}{P_1} &= \sin^2(\Delta\Phi/2) \\ \frac{P_4}{P_1} &= \cos^2(\Delta\Phi/2) \end{aligned} \tag{2.50}$$

where, $\Delta\Phi = (\beta_{00} - \beta_{01})L$ is the relative phase difference between the two guided modes. Using equation (2.49), equation (2.50) can be written as

$$\begin{aligned} \frac{P_3}{P_1} &= \sin^2(\pi L/2L_\pi) \\ \frac{P_4}{P_1} &= \cos^2(\pi L/2L_\pi) \end{aligned} \tag{2.51}$$

Power transferred from input access waveguide-1 to output access waveguide-2 will be maximum when $L = (2p-1)L_\pi$ and minimum when $L = (2p)L_\pi$ where, $p = 1, 2, 3.....$ The first case is referred to as cross state coupling, whereas the second case is known as bar state coupling.

2.3.4 Comparison of beat length of DC, TMI and MMI

Till date, various methods have been used to study coupling characteristics of planar waveguide couplers. Such methods include effective index method [45], Marcatilis method [46], Mercuse method [47], BPM method [48] etc. Among these waveguide design tools, effective index method is simple and can be easily used, with less numerical calculations [49].

Effective index method

Simple effective index method (SEIM) is an analytical waveguide design tool in which, a two dimensional waveguide is approximated by a one dimensional waveguide. The effective index profile of the one dimensional waveguide is same as that of the original structure. There are two possible ways to apply the simple effective index method - SEIM-x method and SEIM-y method [50]. In

SEIM-x method, the effective index method results in a x-dependent refractive index profile, whereas in SEIM-y method, the effective index method results in a y-dependent refractive index profile [45]. Fig-2.11 shows the two dimensional

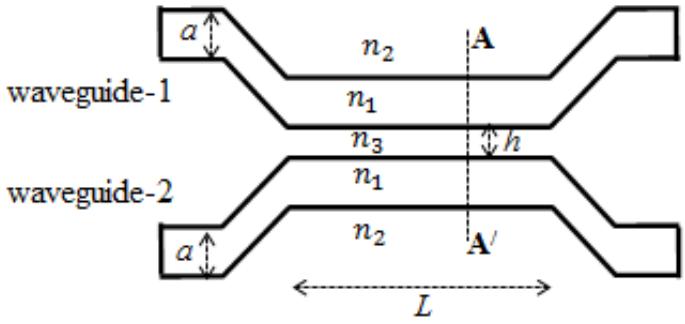

(a) Top view

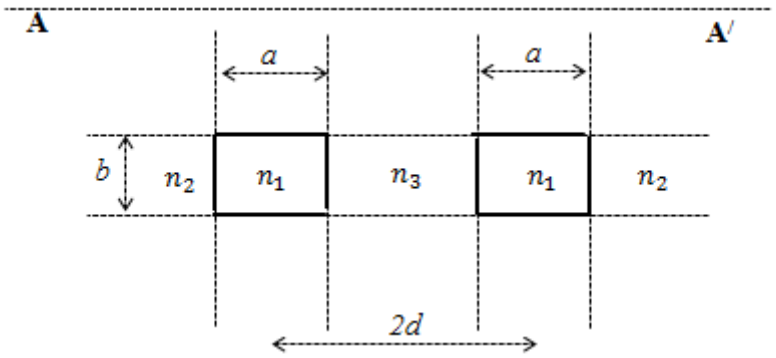

(b) Cross sectional view along the line $AA^{/}$

Figure 2.11: 2D schematic view of an optical directional coupler with identical waveguides

schematic view of an optical directional coupler with identical waveguides having core width a, core thickness b and separated by a gap h. n_1 and n_2 are the refractive indices of core and surrounding cladding respectively, whereas n_3 is the refractive index of the gap of separation.

Fig-2.12 shows the SEIM-x method for simplifying the refractive index profile of the directional coupler shown in Fig-2.11. It is seen that, the refractive index of the cladding region in both the waveguides differs from the original by a small amount. In both sides of the core, the refractive index increases by an amount of $(n_1^2 - n_x^2)$, whereas in the corners, it decreases by $(n_x^2 - n_2^2)$.

Fig-2.13 shows the SEIM-y method for studying the refractive index profile of the directional coupler shown in Fig-2.11. In this case, the refractive index of the cladding region above and below the core in both waveguides increases by an amount $(n_1^2 - n_y^2)$, whereas, in the corners, the refractive index decreases. We

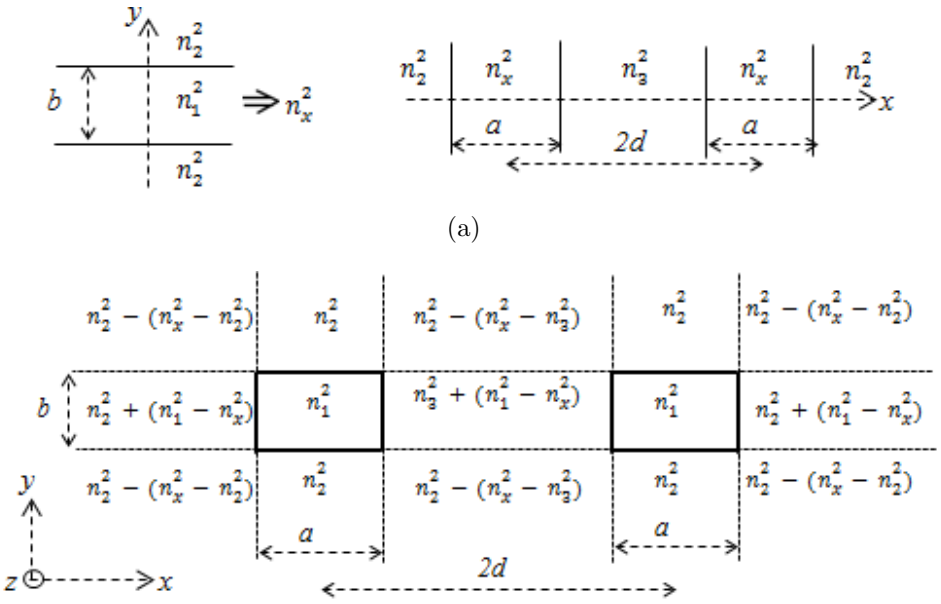

Figure 2.12: Schematic representation of simple effective index method along x-direction (SEIM-x).

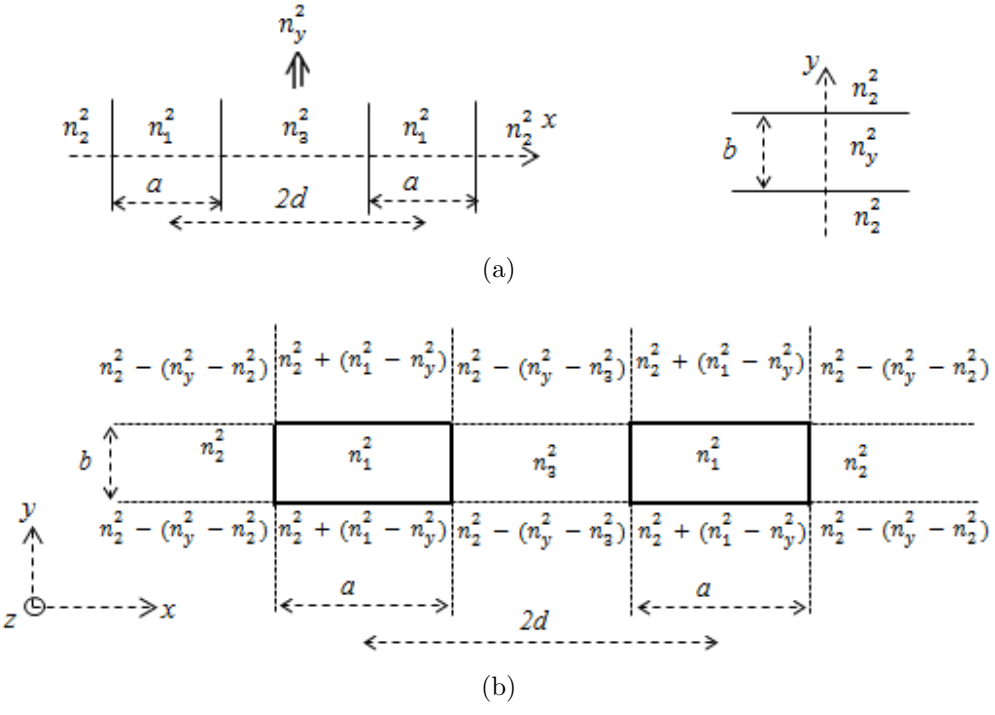

Figure 2.13: Schematic representation of simple effective index method along y-direction (SEIM-y).

have analyzed the coupling characteristics of the optical directional coupler with the help of SEIM-x method in order to study its characteristics with respect to those of optical TMI coupler and optical MMI coupler.

Beat length of directional coupler

With the help of coupled mode theory, the normalized coupling coefficients can be written as [49, 50]

$$\frac{C}{C_0} = \frac{V\int_{-b/2}^{b/2}\int_{d-a/2}^{d+a/2}\Psi_0(x+d,y)\Psi_0(x-d,y)dxdy}{2\int_{-\infty}^{\infty}\int_{-\infty}^{\infty}\Psi_0^2(x,y)dxdy} \tag{2.52}$$

where

$$C_0 = \frac{0.4}{1+0.2h} \times \frac{(n_1^2-n_{eff}^2)\sqrt{n_{eff}^2-n_2^2}}{n_{eff}(n_1^2-n_3^2)\left[W+\frac{2}{k_0\sqrt{n_{eff}^2-n_2^2}}\right]} \tag{2.53}$$

and

$$V = \frac{bk_0}{2}\sqrt{n_1^2-n_3^2} \quad , \qquad k_0 = 2\pi/\lambda \tag{2.54}$$

$\Psi_0(x,y)$ is the mode field of a single rectangular core waveguide. Using asymptotic consideration [50], $\Psi_0(x,y)$ can be written as the following:

For core region,

$$\Psi_0(x,y) = \sin\left(\frac{\pi(x+a/2)}{a}\right)\sin\left(\frac{\pi(y+b/2)}{b}\right); |x| < \frac{a}{2}, |y| < \frac{b}{2} \tag{2.55}$$

and for different cladding regions,

$$\Psi_0(x,y) = \begin{cases} \frac{\pi b}{2aV_1}\sin\left(\frac{\pi(y+b/2)}{b}\right)\exp\left(-V_1\frac{|x|-a/2}{b/2}\right) & ; -\infty \le x \le -\frac{a}{2}, \\ & \quad |y| \le \frac{b}{2} \\ \frac{\pi b}{2aV_2}\sin\left(\frac{\pi(y+b/2)}{b}\right)\exp\left(-V_2\frac{|x|-a/2}{b/2}\right) & ; \frac{a}{2} \le x \le \infty, \\ & \quad |y| \le \frac{b}{2} \\ \frac{\pi^2 b}{4aV_1^2}\exp\left(-V_1\frac{|x|-a/2}{b/2}\right)\exp\left(-V_1\frac{|y|-b/2}{b/2}\right) & ; -\infty < x < -\frac{a}{2}, \\ & \quad \frac{b}{2} \le |y| < \infty \\ \frac{\pi^2 b}{4aV_2^2}\exp\left(-V_2\frac{|x|-a/2}{b/2}\right)\exp\left(-V_2\frac{|y|-b/2}{b/2}\right) & ; \frac{a}{2} \le x < \infty, \\ & \quad \frac{b}{2} \le |y| < \infty \\ \frac{\pi}{2V_1}\sin\left(\frac{\pi(x+a/2)}{a}\right)\exp\left(-V_1\frac{|y|-b/2}{b/2}\right) & ; |x| \le \frac{a}{2}, \\ & \quad \frac{b}{2} \le |y| < \infty \end{cases} \tag{2.56}$$

where,

$$V_1 = \frac{bk_0}{2}\sqrt{n_1^2-n_2^2} \quad , \qquad V_2 = \frac{bk_0}{2}\sqrt{n_1^2-n_3^2} \tag{2.57}$$

For a directional coupler, equation (2.52) can be written as

$$\begin{aligned}\frac{C}{C_0} =& \frac{V_1 \int_{-b/2}^{b/2}\int_{d-a/2}^{d+a/2} \Psi_0(x+d,y)\Psi_0(x-d,y)dxdy}{2\int_{-\infty}^{\infty}\int_{-\infty}^{\infty}\Psi_0^2(x,y)dxdy} \\ &+ \frac{V_2 \int_{-b/2}^{b/2}\int_{d-a/2}^{d+a/2} \Psi_0(x+d,y)\Psi_0(x-d,y)dxdy}{2\int_{-\infty}^{\infty}\int_{-\infty}^{\infty}\Psi_0^2(x,y)dxdy}\end{aligned} \tag{2.58}$$

Using equation (2.55) and (2.56) in equation (2.58) and integrating within appropriate boundary limits, we get

$$\begin{aligned}\frac{C}{C_0} &= \frac{V_1}{2ab}\int_{-b/2}^{b/2}\int_{d-a/2}^{d+a/2} \Psi_0(x+d,y)\Psi_0(x-d,y)dxdy \\ &+ \frac{V_2}{2ab}\int_{-b/2}^{b/2}\int_{d-a/2}^{d+a/2} \Psi_0(x+d,y)\Psi_0(x-d,y)dxdy \\ \text{or,}\quad \frac{C}{C_0} &= \frac{V_1}{2ab}\left(\frac{\pi b}{2aV_1}\right)^2 \frac{b}{2}\left(\frac{-b}{4V_1}\right)\left[\exp\left(\frac{-4V_1 d}{b}\right) - \exp\left(\frac{-4V_1(d-a)}{b}\right)\right] \\ &+ \frac{V_2}{2ab}\left(\frac{\pi b}{2aV_2}\right)^2 \frac{b}{2}\left(\frac{-b}{4V_2}\right)\left[\exp\left(\frac{-4V_2 d}{b}\right) - \exp\left(\frac{-4V_2(d-a)}{b}\right)\right] \\ \text{or,}\quad \frac{C}{C_0} &= \left(\frac{-\pi^2 b^3}{64a^3V_1^2}\right)\left[\exp\left(\frac{-4V_1 d}{b}\right) - \exp\left(\frac{-4V_1(d-a)}{b}\right)\right] \\ &+ \left(\frac{-\pi^2 b^3}{64a^3V_2^2}\right)\left[\exp\left(\frac{-4V_2 d}{b}\right) - \exp\left(\frac{-4V_2(d-a)}{b}\right)\right] \\ \text{or,}\quad \frac{C}{C_0} &= \frac{\pi^2 b^3}{64a^3V_1^2}\left[\exp\left(\frac{-4V_1(d-a)}{b}\right) - \exp\left(\frac{-4V_1 d}{b}\right)\right] \\ &+ \frac{\pi^2 b^3}{64a^3V_2^2}\left[\exp\left(\frac{-4V_2(d-a)}{b}\right) - \exp\left(\frac{-4V_2 d}{b}\right)\right]\end{aligned} \tag{2.59}$$

From Fig-2.11(b), we have $2d = a + h$. Substituting $d = (a+h)/2$ in equation (2.59), we obtain

$$\begin{aligned}\frac{C}{C_0} &= \frac{\pi^2 b^3}{64a^3V_1^2}\left[\exp\left(\frac{-2V_1(h-a)}{b}\right) - \exp\left(\frac{-2V_1(h+a)}{b}\right)\right] \\ &+ \frac{\pi^2 b^3}{64a^3V_2^2}\left[\exp\left(\frac{-2V_2(h-a)}{b}\right) - \exp\left(\frac{-2V_2(h+a)}{b}\right)\right] \\ \text{or,}\quad \frac{C}{C_0} &= \frac{\pi^2 b^3}{64a^3V_1^2}\exp\left(\frac{-2V_1}{b}h\right)\left[\exp\left(\frac{2V_1 a}{b}\right) - \exp\left(\frac{-2V_1 a}{b}\right)\right] \\ &+ \frac{\pi^2 b^3}{64a^3V_2^2}\exp\left(\frac{-2V_2}{b}h\right)\left[\exp\left(\frac{2V_2 a}{b}\right) - \exp\left(\frac{-2V_2 a}{b}\right)\right]\end{aligned}$$

$$\text{or,} \quad \frac{C}{C_0} = \frac{\pi^2 b^3}{64a^3}\left[\frac{1}{V_1^2}\exp\left(\frac{-2V_1}{b}h\right)\left[\exp\left(\frac{2V_1 a}{b}\right)-\exp\left(-\frac{2V_1 a}{b}\right)\right] + \frac{1}{V_2^2}\exp\left(\frac{-2V_2}{b}h\right)\left[\exp\left(\frac{2V_2 a}{b}\right)-\exp\left(-\frac{2V_2 a}{b}\right)\right]\right] \quad (2.60)$$

Equation (2.60) gives the generalized expression for the normalized coupling coefficient for an optical directional coupler. Considering a square embedded channel waveguide for which $a = b$ and substituting V_1 and V_2 from equation (2.57) in equation (2.60), we get

$$\frac{C}{C_0} = \frac{\pi^2}{16b^2k_0^2\left(n_1^2-n_2^2\right)}\exp\left(-hk_0\sqrt{n_{eff}^2-n_2^2}\right)\left[\exp\left(bk_0\sqrt{n_1^2-n_2^2}\right)-\exp\left(-bk_0\sqrt{n_1^2-n_2^2}\right)\right] + \frac{\pi^2}{16b^2k_0^2\left(n_1^2-n_3^2\right)}\exp\left(-hk_0\sqrt{n_{eff}^2-n_3^2}\right)\left[\exp\left(bk_0\sqrt{n_1^2-n_3^2}\right)-\exp\left(-bk_0\sqrt{n_1^2-n_3^2}\right)\right] \quad (2.61)$$

where, n_{eff} is the effective refractive index calculated using simple effective index method and can be written as

$$n_{eff} = \beta\left(\frac{\lambda}{2\pi}\right) \quad (2.62)$$

The propagation constant β can be estimated using dispersion relations [36] of a rectangular core waveguide as follows:

Fig-2.14 shows a basic optical waveguide structure consisting of three layers: core layer with width W, thickness T and refractive index n_{core}, and the cladding and substrate layers with refractive indices n_{clad} and n_{sub} respectively. For a two dimensional step-index planar waveguide, the dispersion equation along x-axis can be written as

$$V_I\sqrt{1-b_I} = (m+1)\pi - \tan^{-1}\sqrt{\frac{1-b_I}{b_I}} - \tan^{-1}\sqrt{\frac{1-b_I}{b_I+a_I}} \quad (2.63)$$

where, m is an integer. V_I, b_I and a_I are the normalized frequency, normalized guide index and asymmetric factor of the waveguide structure respectively and

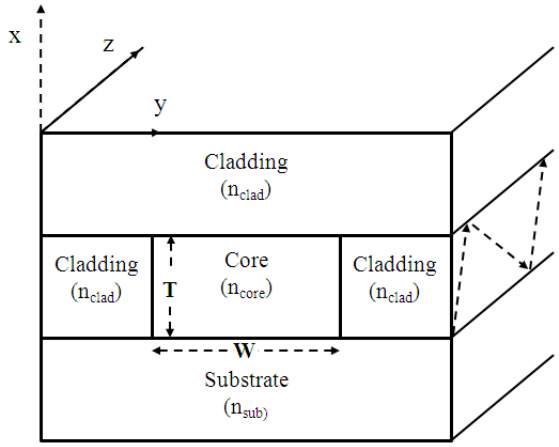

Figure 2.14: Basic optical waveguide structure consisting of core layer with width W, thickness T and refractive index n_{core}, cladding layer with refractive index n_{clad} and substrate layer with refractive index n_{sub}

can be written as

$$\begin{aligned} V_I &= k_0 T \sqrt{n_{core}^2 - n_{sub}^2} \\ b_I &= \frac{N^{/2} - n_{sub}^2}{n_{core}^2 - n_{sub}^2} \\ a_I &= \frac{n_{sub}^2 - n_{clad}^2}{n_{core}^2 - n_{sub}^2} \end{aligned} \tag{2.64}$$

Here, $N^{/}$ is the effective index along x-direction. For a symmetric two dimensional planar waveguide, $n_{clad} = n_{sub}$ and $a_I = 0$. Thus the dispersion equation (2.63) reduces to

$$V_I \sqrt{1 - b_I} = (m+1)\pi - 2\tan^{-1}\sqrt{\frac{1-b_I}{b_I}} \tag{2.65}$$

Substituting value of b_I which satisfies equation (2.65) into equation (2.64), $N^{/}$ can be estimated as

$$N^{/} = \sqrt{n_{clad}^2 + b_I(n_{core}^2 - n_{clad}^2)} \tag{2.66}$$

Dispersion equation along y-axis for the waveguide shown in Fig-2.14, can be written as

$$V_{II} \sqrt{1 - b_{II}} = (n+1)\pi - 2\tan^{-1}\sqrt{\frac{1-b_{II}}{b_{II}}} \tag{2.67}$$

where, n is an integer. V_{II} and b_{II} are the normalized frequency and normalized

guide index respectively and can be written as

$$\begin{aligned} V_{II} &= k_0 W \sqrt{N/2 - n_{clad}^2} \\ b_{II} &= \frac{n_{eff}^2 - n_{clad}^2}{N/2 - n_{clad}^2} \end{aligned} \tag{2.68}$$

From equation (2.68), n_{eff} can be written as

$$n_{eff} = \sqrt{n_{clad}^2 + b_{II}(N/2 - n_{clad}^2)} \tag{2.69}$$

Substituting values of b_{II} that satisfies equation (2.68) into equation (2.69), n_{eff} can be calculated. Equation (2.69) along with equation (2.53) and equation (2.61) gives the normalized coupling coefficients of the rectangular core directional coupler.

The beat length of a directional coupler is defined as the propagation distance at which the phase shift between the even and odd modes propagating through the coupling region becomes π. It can be written as

$$L_\pi = \frac{\pi}{(\beta_e - \beta_o)} = \frac{\pi}{2C} \tag{2.70}$$

where, β_e and β_o are the propagation constants of the even and odd mode propagating along the directional coupler. C is the coupling coefficient of the directional coupler, determined by using equations (2.53), (2.61) and (2.69).

Fig-2.15 shows the variation of beat length (L_π) of an optical directional coupler obtained by using a SEIM model with respect to the coupling gap (h), for different values of coupling gap refractive indices $n_3 = 1.45$, 1.46, 1.47, 1.48, 1.49 and 1.495. Here, we have chosen $n_1 = 1.5$, $n_2 = 1.45$, $\Delta n = 5\%$, $a = b = 1.5\mu m$ and $\lambda = 1.55\mu m$. It is evident from the figure that the beat length L_π increases with increase in the coupling gap h.

Fig-2.16 shows the behavior for beat length of DC with respect to index contrast (Δn) with $n_2 = n_3 = 1.45$, $a = b = 1.5\mu m$ and $\lambda = 1.55\mu m$ for different values of coupling gap $h = 0.03\mu m$, $0.3\mu m$, $0.55\mu m$ and $1.0\mu m$. From the figure, it is seen that the beat length of the DC decreases with increase in the index contrast, indicating small beat length for high index contrast waveguides. It is found that, beat length of the directional coupler with $n_2 = n_3 = 1.45$, $a = b = 1.5\mu m$, $\lambda = 1.55\mu m$ and $\Delta n = 5\%$ for different coupling gap $h = 0.03\mu m$, $0.3\mu m$, $0.55\mu m$ and $1.0\mu m$ are obtained as $\sim 45\mu m$, $80\mu m$, $96\mu m$ and $140\mu m$

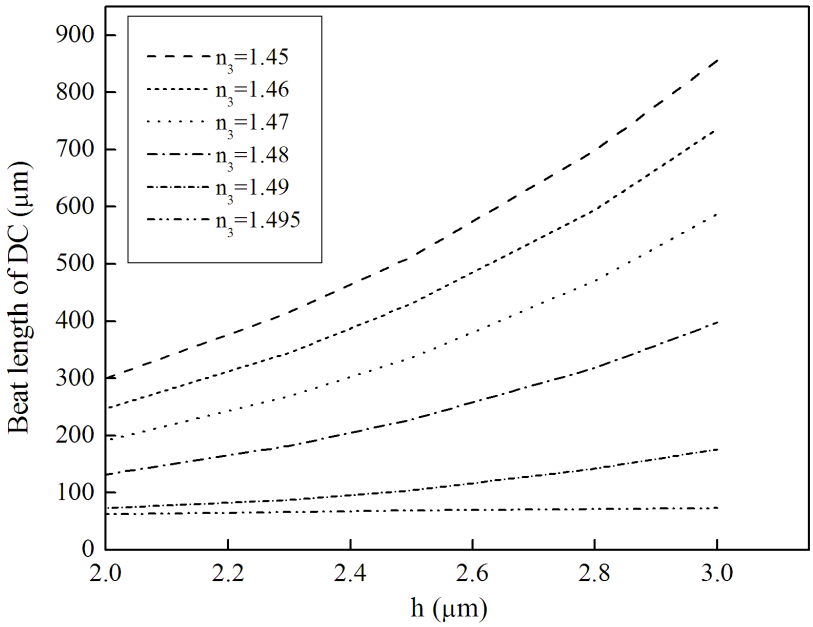

Figure 2.15: Beat length of directional coupler (DC) versus separation gap for coupling gap refractive indices $n_3 = 1.45$, 1.46, 1.47, 1.48, 1.49 and 1.495. $n_1 = 1.5$, $n_2 = 1.45$, $\Delta n = 5\%$, $a = b = 1.5\mu m$ and $\lambda = 1.55\mu m$.

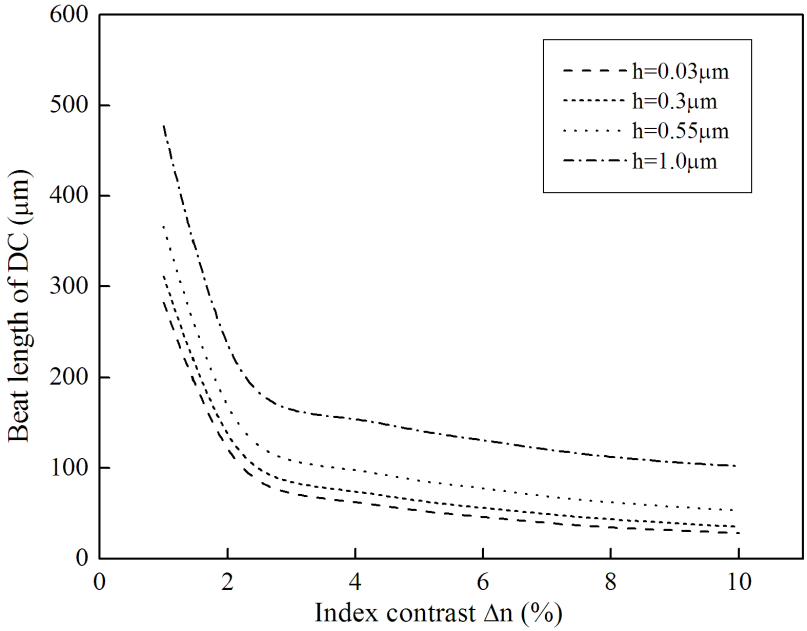

Figure 2.16: Beat length of directional coupler (DC) with index contrast for coupling gap $h = 0.03\mu m$, $0.3\mu m$, $0.55\mu m$ and $1.0\mu m$ with $n_2 = n_3 = 1.45$, $a = b = 1.5\mu m$ and $\lambda = 1.55\mu m$

respectively.

Beat length of TMI coupler

A two-mode interference (TMI) coupler consists of two single mode waveguides placed with zero separation gap. Depending on the phase difference between the excited modes at the end of the coupling region, light energy is obtained at the output access waveguides in cross state or bar state. Fig-2.17 shows the two

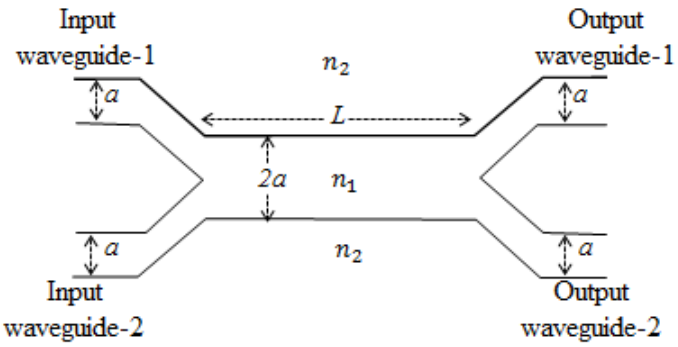

Figure 2.17: Two dimensional schematic view of a TMI coupler

dimensional schematic view of an optical TMI coupler. It consists of two-mode coupling region with core width $2a$, core thickness b (not shown in figure) and coupling length L, and single mode input and output access waveguides with width a and thickness b. The refractive indices of the core and cladding are n_1 and n_2 respectively. When light signal is launched into the coupler through any of the input access waveguides, the fundamental and first order modes are excited in the coupling region with propagation constants β_0 and β_1 respectively. The beat length i.e., the propagation length at which phase difference between the two modes becomes π can be written as

$$L_\pi = \frac{\pi}{\beta_0 - \beta_1} = \frac{\pi}{2C} \tag{2.71}$$

where, C is the coupling coefficient for two-mode interference coupler. It can be calculated from asymptotic analysis of SEIM model of DC discussed earlier, with a consideration of $h \sim 0$.

From the asymptotic analysis of SEIM model, the coupling coefficient of TMI coupler can be calculated with the help of the following equation:

$$\begin{aligned}\frac{C}{C_0} = \frac{\pi^2 b^3}{64a^3}\Bigg[&\frac{1}{V_1^2}\exp\left(\frac{-2V_1}{b}h\right)\left[\exp\left(\frac{2V_1 a}{b}\right) - \exp\left(\frac{-2V_1 a}{b}\right)\right] \\ &+ \frac{1}{V_2^2}\exp\left(\frac{-2V_2}{b}h\right)\left[\exp\left(\frac{2V_2 a}{b}\right) - \exp\left(\frac{-2V_2 a}{b}\right)\right]\Bigg]\end{aligned} \tag{2.72}$$

where,

$$V_1 = \frac{b}{2}k_0\sqrt{n_1^2 - n_2^2} \quad , \qquad V_2 = \frac{b}{2}k_0\sqrt{n_1^2 - n_3^2} \tag{2.73}$$

As h tends to zero ($h \to 0$) for a TMI coupler, the value of the exponential term containing h in equation (2.72) becomes 1. Moreover, since there is no separation between the cores, n_3 does not exist and hence, V_2 vanishes. Thus equation (2.72) can be approximated for a TMI coupler as the following-

$$\frac{C}{C_0} = \frac{\pi^2 b^3}{64a^3V_1^2}\left[\exp\left(\frac{2V_1a}{b}\right) - \exp\left(\frac{-2V_1a}{b}\right)\right] \tag{2.74}$$

Considering a square embedded channel waveguide ($a = b$) and substituting the value of V_1 from equation (2.73), equation (2.74) can be written as

$$\frac{C}{C_0} = \frac{\pi^2}{16b^2k_0^2\left(n_1^2 - n_2^2\right)}\left[\exp\left(bk_0\sqrt{n_1^2 - n_2^2}\right) - \exp\left(-bk_0\sqrt{n_1^2 - n_2^2}\right)\right] \tag{2.75}$$

where, C_0 is given by equation (2.53). Thus, calculating the value of C from equation (2.75) and equation (2.53), the beat length can be calculated from equation (2.71).

The beat length (L_π) of a TMI coupler ($h = 0$) with respect to the index contrast, with $a = b = 1.5\mu m$, $n_2 = 1.45$ and $\lambda = 1.55\mu m$ is shown in Fig-2.18. It is seen from the figure that, as the index contrast increases, beat length of TMI coupler decreases. From the figure, the beat length for $a = b = 1.5\mu m$, $n_2 = 1.45$, $\lambda = 1.55\mu m$ and $\Delta n = 5\%$ is found to be $L_\pi \sim 45\mu m$.

Beat length of MMI coupler

Multimode interference (MMI) couplers consist of two single mode waveguides in such a way that the gap between the waveguides ($h > 0$) in the coupling region is filled with the same core material. Fig-2.19 shows a two dimensional schematic view of a 2×2 MMI coupler with core refractive index n_1 and cladding refractive index n_2. The width and thickness of the single mode access waveguides are a and b (not shown in figure) respectively, whereas the width, thickness and length of the coupling region are $2a + h$, b and L respectively. When light signal is launched into one of the input access waveguides, large number of modes are excited along with fundamental and first order modes, in the coupling region. Depending on the phase difference between the excited modes at the end of the coupling region, the position of the output is decided. The beat length of MMI

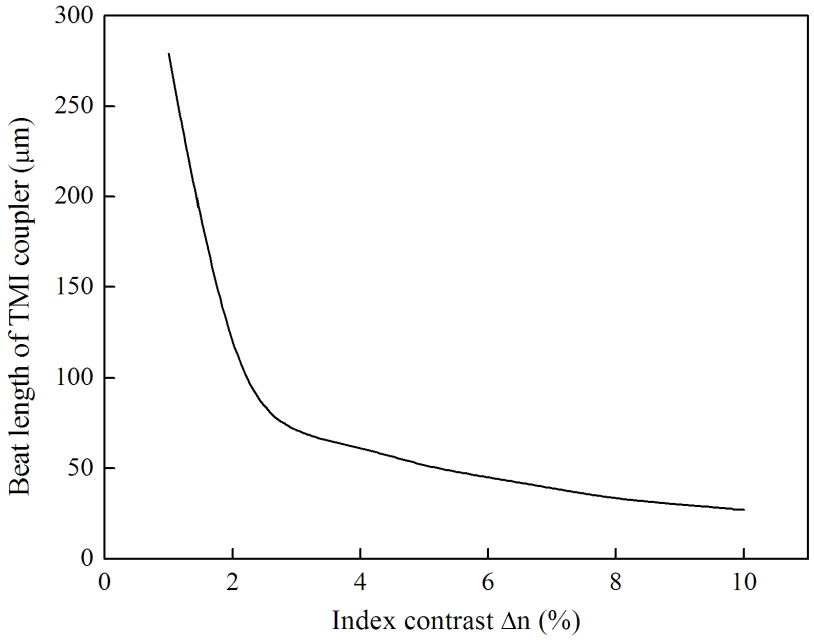

Figure 2.18: Beat length of a TMI coupler versus index contrast with $a = b = 1.5\mu m$, $n_2 = 1.45$ and $\lambda = 1.55\mu m$.

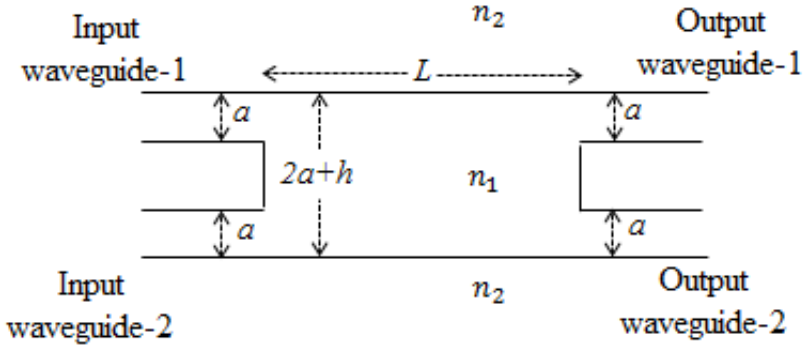

Figure 2.19: Two dimensional schematic view of a 2×2 MMI coupler

coupler can be written as

$$L_\pi = \frac{\pi}{\beta_{00} - \beta_{01}} \tag{2.76}$$

From the asymptotic analysis of SEIM model with the consideration $n_3 \to n_1$, the coupling coefficient of MMI coupler can be calculated with the help of the following equation:

$$\begin{aligned}\frac{C}{C_0} = \frac{\pi^2 b^3}{64a^3}\Bigg[&\frac{1}{V_1^2}\exp\left(\frac{-2V_1}{b}h\right)\left[\exp\left(\frac{2V_1 a}{b}\right) - \exp\left(\frac{-2V_1 a}{b}\right)\right] \\ &+ \frac{1}{V_2^2}\exp\left(\frac{-2V_2}{b}h\right)\left[\exp\left(\frac{2V_2 a}{b}\right) - \exp\left(\frac{-2V_2 a}{b}\right)\right]\Bigg]\end{aligned} \tag{2.77}$$

where,

$$V_1 = \frac{b}{2}k_0\sqrt{n_1^2 - n_2^2} \quad , \qquad V_2 = \frac{b}{2}k_0\sqrt{n_1^2 - n_3^2} \tag{2.78}$$

Using the condition $n_3 \to n_1$ for a MMI coupler, equation (2.77) can be written as

$$\frac{C}{C_0} = \frac{\pi^2 b^3}{64a^3V_1^2}\exp\left(\frac{-2V_1}{b}h\right)\left[\exp\left(\frac{2V_1 a}{b}\right) - \exp\left(\frac{-2V_1 a}{b}\right)\right] \tag{2.79}$$

Using $a = b$ for a square embedded channel waveguide and substituting the value of V_1 from equation (2.78) into equation (2.79), we obtain

$$\begin{aligned}\frac{C}{C_0} =& \frac{\pi^2}{16b^2k_0^2(n_1^2 - n_2^2)}\exp\left(-hk_0\sqrt{n_1^2 - n_2^2}\right)\left[\exp\left(bk_0\sqrt{n_1^2 - n_2^2}\right)\right. \\ & \left. - \exp\left(-bk_0\sqrt{n_1^2 - n_2^2}\right)\right]\end{aligned} \tag{2.80}$$

where C_0 is given by equation (2.53). Thus, using equations (2.53), (2.76) and (2.80), the value of beat length for optical MMI coupler can be calculated.

Beat length of an optical MMI coupler with respect to the coupling gap, with $n_1 = 1.5$, $n_2 = 1.45$, $\Delta n = 5\%$, $a = b = 1.5\mu m$, and $\lambda = 1.55\mu m$ has been shown in Fig-2.20. It is seen from the figure that beat length of MMI coupler increases with increase in the coupling gap. This occurs due to the fact that,

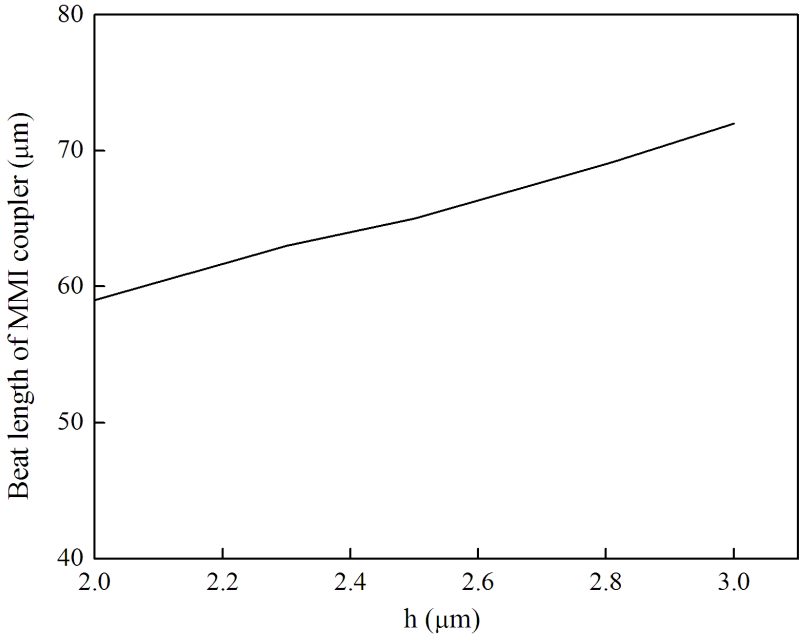

Figure 2.20: Beat length of a MMI coupler versus separation gap h, with $n_1 = 1.5$, $n_2 = 1.45$, $\Delta n = 5\%$, $a = b = 1.5\mu m$, and $\lambda = 1.55\mu m$.

with increase in the coupling gap, higher order modes are excited in the MMI region.

Fig-2.21 shows variation of beat length of MMI coupler with increase in the index contrast, for $n_2 = 1.45$, $a = b = 1.5\mu m$ and $\lambda = 1.55\mu m$. It is evident from the figure that, the higher is the index contrast, the smaller is the beat length.

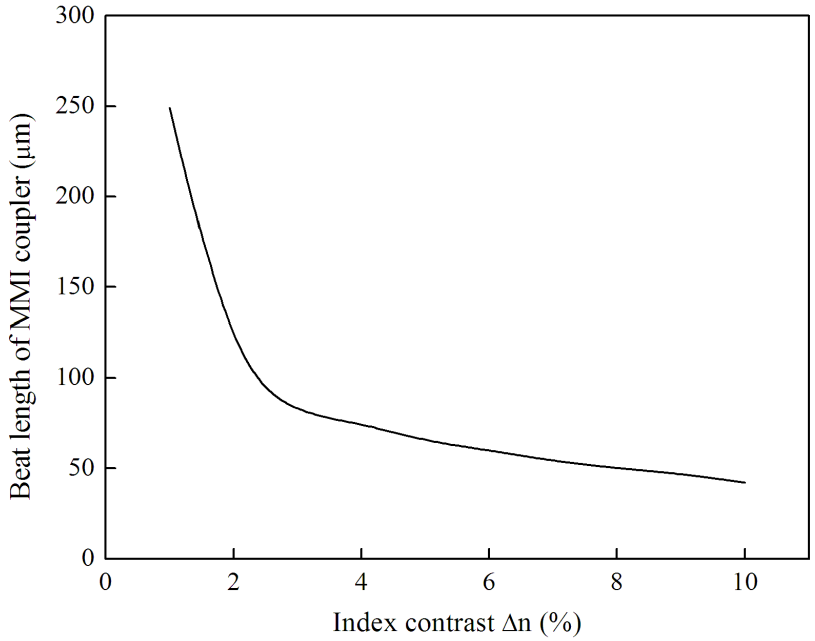

Figure 2.21: Beat length of a MMI coupler versus index contrast with $n_2 = 1.45$, $a = b = 1.5\mu m$ and $\lambda = 1.55\mu m$

Comparison of DC, TMI and MMI coupler

Fig-2.22 shows a comparison between beat length of directional coupler with $a = b = 1.5\mu m$ and different coupling gap refractive indices $n_3 = 1.45$, 1.47, 1.49 and 1.495, and MMI coupler with $a = b = 1.5\mu m$ and $\Delta n = 5\%$ at wavelength $\lambda = 1.55\mu m$. From the figure, it is seen that beat length of DC for $n_3 = 1.45$ is much higher than that of MMI coupler and as n_3 increases, beat length of DC decreases. As n_3 approaches n_1, the curves for DC become closer and closer, and for $n_3 = 1.495$, the curve is almost superposed with that of MMI coupler. Moreover, when the curves for DC and MMI are extrapolated to meet the y-axis ($h = 0$), they tend to meet at the same point at the y-axis given by $L_\pi \sim 45\mu m$ which is the beat length of TMI coupler having $\Delta n = 5\%$ and $a = b = 1.5\mu m$ at wavelength $\lambda = 1.55\mu m$.

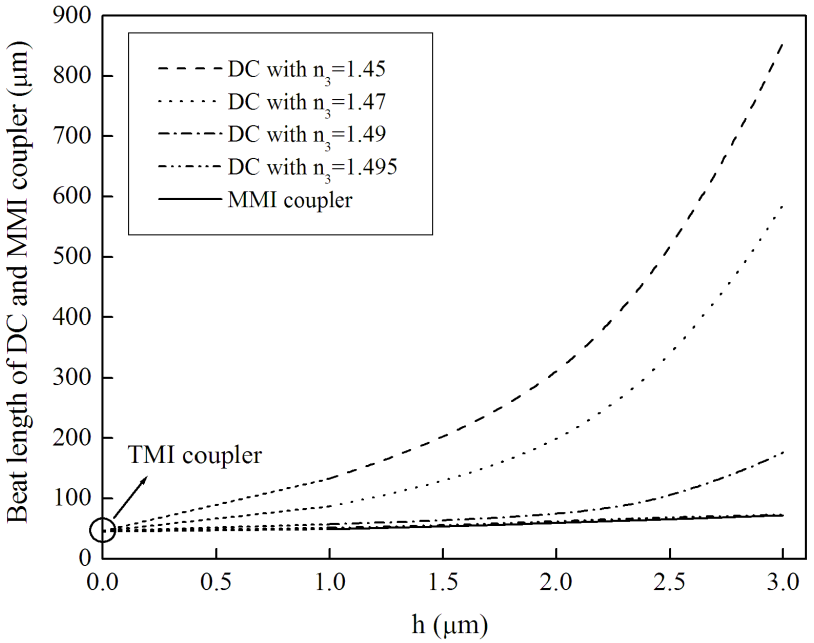

Figure 2.22: Beat length versus h of directional coupler with $a = b = 1.5\mu m$ and different coupling gap refractive indices $n_3 = 1.45$, 1.47, 1.49 and 1.495 (dotted curves), and MMI coupler with $a = b = 1.5\mu m$ and $\Delta n = 5\%$ (solid curve) at wavelength $\lambda = 1.55\mu m$.

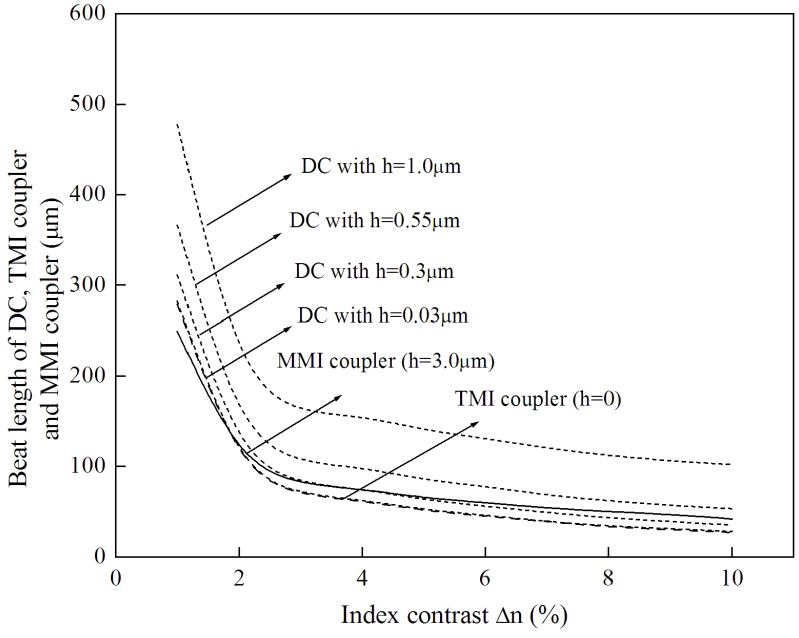

Figure 2.23: Beat length versus index contrast for directional coupler with different coupling gap $h = 0.03\mu m$, $0.3\mu m$, $0.55\mu m$ and $1.0\mu m$, TMI coupler ($h = 0$) and MMI coupler with $h = 3.0\mu m$. Here, $n_2 = 1.45$, $a = b = 1.5\mu m$ and $\lambda = 1.55\mu m$.

Fig-2.23 shows beat lengths versus index contrast for TMI coupler ($h = 0$), MMI coupler with $h = 3.0\mu m$ and directional coupler with different coupling gap $h = 0.03\mu m$, $0.3\mu m$, $0.55\mu m$ and $1.0\mu m$. It is seen from the figure that beat length decreases with increase in the index contrast, the rate of decrease being high for $\Delta n \leq 2\%$ and slower for $\Delta n > 2\%$, for all the curves. It is also seen that, curve for beat length of DC for $h = 1.0\mu m$ is much higher than that of TMI coupler, but the curve becomes closer as h decreases. For $h \leq 0.03\mu m$, the curves for DC and TMI coupler are almost superposed.

From Fig-2.22 and Fig-2.23, one can arrive at the following conclusions:

1. Waveguide couplers with higher index contrast have smaller beat length.
2. Beat length of TMI coupler is the smallest as compared to directional coupler and MMI coupler.
3. When the refractive index of the coupling gap n_3 approaches the core refractive index n_1 ($n_3 \rightarrow n_1$), directional couplers show characteristics equivalent to those of multimode interference couplers.
4. When the coupling gap h decreases ($h \leq 0.02\mu m$), DC shows characteristics equivalent to MMI coupler. As h approaches zero ($h \rightarrow 0$), both DC and MMI coupler show characteristics equivalent to those of TMI couplers.

2.4 Review on all-optical waveguide devices

In this section, we have discussed some previously reported waveguide devices based on multimode interference coupling in surface plasmonic waveguide. With an aim to provide a strong foundation to appreciate the designs proposed in this thesis, we have also discussed some previously reported works on all-optical logic gates and optical power splitters. The later part of the section gives a brief idea of the loss occurring in bent waveguides used in access waveguide portion of the multimode waveguides and the KCl:$Tl^0(1)$ laser used for applying optical pulse at nonlinear cladding region in our proposed device.

2.4.1 Multimode interference (MMI) waveguide structures based on Surface plasmon polariton (SPP)

During the last two decades, there has been extensive theoretical as well as experimental research in the field of SPP devices based on MMI principle. Use of MMI based SPP devices have given a new direction to the study of integrated optic devices. Most of the previous works report compact power splitter devices while a few works report optical switches and other optoelectronic devices.

In 2005, A. Boltasseva *et al.* [51] reported MMI device based on long-range SPP stripe waveguides to perform the function of power splitting at a wavelength of $\lambda = 1.55\mu m$. The basic structure used in this work was a stripe waveguide in which a gold stripe (refractive index=$0.55 + j11.5$) is surrounded by two identical layers of the Benzocyclobutene polymer (refractive index=1.535). Taking various width of the gold stripe, Boltasseva has experimentally depicted the formation of two-fold images and four-fold images in accordance with the MMI principle.

In 2006, R. Zia *et al.* [20] studied SPP propagation in stripe waveguides consisting of gold stripes of different width placed on glass substrate and experimentally demonstrated two-mode and multimode propagation in an SPP waveguide. The results revealed a beating in the direction of propagation when the fundamental and first order modes are excited simultaneously. The experimental value of beat length obtained by Zia was found to be in good agreement with the value obtained from numerical simulations. His work also demonstrates that the propagation of light in an SPP waveguide takes place by the formation of discrete guided modes as well as continuous radiation modes.

In 2007, Z. Han *et al.* reported a 1×N MMI splitter with ultra-compact transverse size based on index guided multimode plasmonic waveguide (IGMPW) with silver, silicon (core dielectric) and air (second dielectric) [52, 53]. The 1×2 power splitter designed by them was found to have a transverse size of the order of one third of the working wavelength $\lambda = 1.55\mu m$ ($\approx 500nm$). However, the power splitting ratio of the device depends on the device geometry. For a particular device, the power splitting ratio is fixed once the device has been fabricated.

In 2008, S. Passinger *et al.* proposed a DLSPP waveguide Y-splitter based on multimode propagation to address the issues of scattering of light leading to excess losses in the branching area [54]. An ultra-compact size was achieved

with a broad splitting ratio tuning range depending on the length of the cut section and without any significant increase of the excess losses.

In the year 2009, SPP based MMI waveguide devices were demonstrated by Y. J. Tsai *et al.* [55] using wide metal stripes and by G. Yuan *et al.* [56] using DLSPP waveguide. Y. J. Tsai *et al.* [55] fabricated the stripe based MMI couplers and demonstrated the self-imaging principle experimentally. However, the MMI coupler suffered from very large size of the order of hundreds of micrometers. Yuan *et al.* [56] numerically demonstrated 1×N MMI splitters based on DLSPP waveguides and achieved compact size of the order of micrometers.

J. Wang *et al.* [57] in 2011, proposed optical power splitters based on multimode interference in silicon hybrid plasmonic waveguides and demonstrated optical power splitting ratio variation in the range from 97.1% : 2.9% to 1.7% : 98.3% by varying the length of the device based on two-mode interference coupling. In the same year, Y. Kou *et al.* [58] investigated and numerically demonstrated MMI effect in multimode MIM waveguides and observed beat length of the order of micrometers. In 2013, Z. Zhu *et al.* [59] demonstrated MMI coupling in dielectric-loaded surface plasmon polariton waveguides and achieved 1×2 beam splitting and demultiplexing function for a length of only several micrometers.

It is clear from the above literature that, very few literature is available on SPP based two-mode interference waveguide component for integrated optical processor devices.

2.4.2 All-optical logic gates

High performance all-optical logic gates have become key components in optical computing and networking systems to perform optical signal processing functions such as binary addition, parity checking, header reorganization, all-optical label swapping and data encryption [10]. Efforts to realize all-optical logic gates have started a long time ago since the 1980s [60–62]. Since then, all-optical logic gates have been realized using various approaches such as directional couplers [63–65], two-mode interference (TMI) couplers [66, 67], multimode interference (MMI) couplers [68–71], nonlinear photonic crystals [72, 73], semiconductor optical amplifier (SOA) [74–76], highly nonlinear fiber [77, 78], surface plasmon polariton (SPP) [26,27,79–85] etc. While some of the reported works could implement only single or few logic functions, some were found to have larger device dimensions.

Because it is impractical to design any optical device having different gates based on different technology, it is necessary to implement all the gates using the same technique. Considerable progress has been made in the research for all-optical logic devices during the last decade. Few remarkable approaches made in the last few years to realize all-optical logic operation for integrated optical processor devices are discussed below:

In 2010, Hong Wei *et al.* [79] reported SPP based interferometric logic gates in silver nanowire networks. Using an imaging strategy based on quantum dots, fundamental logic gates NOT, OR AND, NAND and XOR were implemented. Next year, Hong Wei *et al.* [80] implemented the NOR gate by cascading OR and NOT gates based on the same technology. These logic devices are based on interference of light and depend on relative optical phase difference between the various input optical signals. This causes an inherent instability due to difficulties in precise control of the optical phase difference.

In 2011, Y. Ishizaka *et al.* [70] proposed ultra-compact all-optical logic gates using photonic crystal waveguides based on multi-mode interference devices. The implemented logic gates were found to be ultra-compact in size ($9.9\mu m \times 10.8\mu m$) with a low power consumption. However, only the AND and XOR logic operations were implemented using the structure. In the same year, C. Husko *et al.* [86] demonstrated a chip-based, all-optical XOR logic gate by using slow-light enhanced four-wave mixing (FWM) in silicon photonic crystal waveguide (PhCWG). The implemented gate was found to have a device length of $396\mu m$. Moreover, only a single logic operation (XOR) could be realized by using their proposed structure.

In the year 2012, E. Dimitriadou *et al.* [87] proposed a new structure for all-optical logic gates by using quantum-dot SOA-based MZ interferometer. But this structure could implement only the NOT logic operation. Later in the same year, E. Dimitriadou *et al.* [88] proposed all-optical NOR logic gates by using single quantum-dot SOA-based MZ interferometer. Even then, only the NOT and NOR operations were realized using their proposed structure.

There were more approaches for all-optical logic operations using SPP propagation such as using air slots cut in a thin gold film [27] by Y. Fu. *et al.* in 2012, using Y-shaped ferroelectric hybrid plasmonic waveguide [81] by C. Lu *et al.* in 2013 and using air slots etched on a silver film with an Y-shaped junction [26] by D. Pan *et al.* in 2013. Although these devices based on linear interference achieve a compact device dimension but the problem of instability

owing to difficulties in precise control of phase difference of input signal was still persistent. Moreover, in the work reported by Deng Pan *et al.* [26], the threshold intensity value for obtaining logic high and low states varies with type of gate realized. This may be a point of concern while combining large number of gates to make optical processor.

In 2013, W Liu *et al.* [89] designed ultra-compact all-optical logic gates by using MMI waveguide based on photonic waveguide and realized. Using their proposed structure, XOR, XNOR, NAND and OR gates could be designed. But, the definition of input logic states for the gates depend on the phase of input signal and also, is different for different gates which may be a problem for larger circuits involving a large number of gates. In the same year, Yaw-Dong Wu *et al.* [82] demonstrated all-optical logic operation using microring metal-insulator-metal (MIM) plasmonic waveguides in which switching of logic states are achieved via coupling between straight waveguides and ring resonator waveguides. However, only the NOT logic operation was achieved by using this structure.

Recently in 2014, A. Fushimi *et al.* [90] proposed all-optical logic gates based on cavity system, operated using a single wavelength laser and realized OR, AND, NOR and NAND gates. However, the proposed gates were found to have different configuration, and also, the device size for various gates range from $120\mu m$ to $400\mu m$. In the same year, J. Bao *et al.* [91] demonstrated all-optical logic gates by using photonic crystal ring resonator. But, only the NOR and NAND gates were realized using the structure.

Recently in 2015, Wenyu Zhao *et al.* [83] have demonstrated all-optical logic gates based on a plasmonic ring resonator using nonlinear material. In this structure, NOT, NAND and NOR logic operations were controlled by optical pulse with different peak intensity. However, complex optical processor needs combination of numerous gates requiring precise control of the intensity of optical pulse to define a logic operation. E. Pourali1 *et al.* [85] have proposed an all-optical OR gate using surface plasmon propagation through gold and silver nanorods in 2015. Although this structure can provide an almost zero cross talk and a dimension of the order of $3\mu m \times 5\mu m$, but only the OR logic operation is obtained by using the structure proposed by them.

2.4.3 Optically tunable power splitter

Compact optical power splitters are indispensable components of integrated optical processor for distribution of power among its building blocks. Fig-2.24 shows

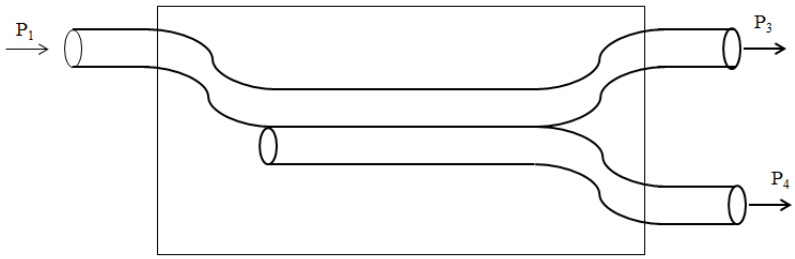

Figure 2.24: Schematic view of a conventional optical power splitter

the schematic view of a conventional optical power splitter with input power P_1 and output powers P_3 and P_4. The output powers P_3 and P_4 can be expressed in terms of the input power P_1 by the following relations:

$$\begin{aligned} P_3 &= \alpha_1 P_1 \\ P_4 &= \alpha_2 P_1 \end{aligned} \tag{2.81}$$

where, α_1 and α_2 are constants depending on the device architecture. The splitting ratio of the device is given by $\alpha_1 : \alpha_2$ and the optical power splitter is known as a $\alpha_1 : \alpha_2$ splitter. In the ideal case i.e., no loss, $\alpha_1 + \alpha_2 = 1$ so that, $P_3 + P_4 = P_1$. The 3dB splitter is a special case of optical power splitter in which, $\alpha_1 = \alpha_2 = 0.5$ and $P_3 = P_4 = P_1/2$.

Tunable optical power splitters are useful for dynamical redistribution and efficient management of optical power in various optoelectronic devices. All-optical control of splitting ratio has become essential for faster operation of these devices. During the last decade, there has been considerable progress in the research for optical power splitter devices. Optical power splitters has been reported both with or without using SPP based structures. A large number of surface plasmonic devices can be attributed to the application in optical power splitting.

Various approaches have been adopted to achieve optical power splitting such as microprism [92], MMI couplers [93–96], microelectromechanical system [97], mode converters [98] as well as surface plasmonic waveguides such as metal-dielectric-metal plasmonic waveguide [99], index guided MIM structure [31, 52], dielectric loaded surface plasmon polariton (DLSPP) waveguide [100], Y-branch

[57], MIM directional coupler [101], TMI coupler [57] , slot cavity [102], ring resonator [103–105], nano rod [106] etc. But in most of the reported works, the power splitting ratio is either fixed [31, 52, 99, 100, 102–104, 106] or can be varied by variation of the device dimensions [57, 102, 105] or manually tuned [92, 96, 98], whereas some or the reported works suffered from larger device dimensions [93, 94, 97, 98], selective values of splitting ratio [95, 103], narrow tuning range [92] etc.

The optical power splitter proposed by Z, Han *et al.* [31] in 2007 using index guided MIM plasmonic waveguide offered an ultra-compact device size, but the tunability of splitting ratio could not be obtained by their proposed structure. In the same year, S. Y. Tseng *et al.* [93] proposed power splitter with variable splitting ratio by using 2×2 MMI coupler, but the structure suffered from larger device dimensions (thousands of micrometers).

The MMI coupler based power splitter proposed by D. J. Feng *et al.* [94] in 2008 to achieve any arbitrary power splitting ratio also suffered from the same disadvantage of larger device size (of the order of a few hundreds of micrometers). In the same year, Q. Chen *et al.* [97] proposed a multifunctional optical device (MFOD) for power splitting, switching etc. The dimensions of this MFOD chip was obtained as $10mm \times 4mm$.

In the year 2011, J. Wang *et al.* [57] demonstrated power splitting by using a TMI coupler as well as an asymetric Y-branch based on a silicon hybrid plasmonic waveguides in nanometer dimensions. The nano-scale power splitter designed by them is an Y-branch with MMI phenomenon . The power splitting ratio could be tuned in the range of $97.1\% : 2.9\% - 1.7\% : 98.3\%$ by using a TMI coupler, and between $84\% : 16\% - 16\% : 84\%$ by using an asymmetric Y-branch. However, the variation of splitting ratio can be obtained by varying the length of the devices which proves to be a disadvantage of the structures proposed by them.

In the same year, S. Tao *et al.* [98] proposed an optical power splitter based on spot-size mode converters. With a device size of $200\mu m$, this optical power splitter could achieve variable power splitting ratio by manual tuning.

In 2011, Najmeh Nozhat *et al.* [101] demonstrated power splitting phenomenon using a metal-insulator-metal plasmonic directional coupler in which the splitting ratio is a function of the coupler length and the metal gap thickness which are fixed for a particular fabricated device.

In year 2013, C. D. Truong *et al.* [95] proposed MMI structure based

optical power splitters using silicon waveguides. Although variations in power splitting ratio was achieved, only some discrete value of splitting ratio were obtained by using this structure.

Recently in 2014, M. Cherchi *et al.* [96] demonstrated variable optical power splitter with unconstrained splitting ratios by using compact double-MMI couplers. However, the variation of splitting ratio in the device requires manual variation of device parameters. In the same year 2014, Ting Zhong *et al.* [105] proposed and designed a plasmonic splitter consisting of two parallel waveguides and two resonators- one ring and one semi-ring, to function as tunable power splitter as well as beam splitter. However, tunability can be achieved by varying the wavelength of incident radiation in a narrow range, because the intensity at the output ports is a function of the incident wavelength.

2.4.4 Bent access waveguides of DC, TMI and MMI devices

Waveguides bends are very important in integrated optic devices. In integrated optical devices, bends are usually used as access waveguide portion of directional couplers (DC), two-mode interference (TMI) couplers, multimode interference (MMI) couplers, Y-splitters etc. Bend waveguides are inherently leaky structures [35] in which, optical loss occurs as the various modes propagate along the bend. This optical loss occurs due to the radiation loss taking place from the modal field into the cladding, which is inherent to the bend waveguide. In addition to this, there is a modal transition loss between the straight waveguide and the waveguide bend which occur due to modal profile mismatch. The magnitude of the bending loss depends mostly on the bend radius. The smaller is the bend radius, the larger is the bending loss. On the other hand, sharp bends or bends with small radius are essential for higher packaging density of integrated optic device components which is a requirement for large scale integration of integrated optical devices.

Single bending loss

Fig-2.25 shows the schematic view of a single bend of bending radius R and bending angle ϕ connected to a straight waveguide. The attenuation of the bend

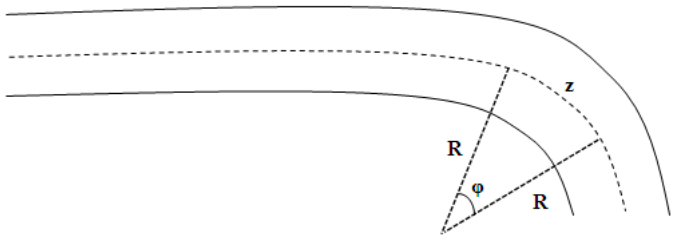

Figure 2.25: Schematic view of a single bend in a waveguide

waveguide for propagation distance z can be expressed as

$$\frac{P_{out}}{P_{in}} = \mathrm{e}^{-(\alpha+\alpha_P)z} \tag{2.82}$$

where, P_{in} =input power, P_{out} =output power, α =bending loss coefficient and α_P =propagation loss coefficient. In bent waveguide, $\alpha >> \alpha_P$. Thus, equation (2.82) can be written as

$$\frac{P_{out}}{P_{in}} = \mathrm{e}^{-\alpha z} \tag{2.83}$$

The bending loss in dB can be expressed as

$$\begin{aligned} T_B &= -10 \log \frac{P_{out}}{P_{in}} \\ &= -\frac{10}{\ln 10} \ln \frac{P_{out}}{P_{in}} \\ &= \frac{10}{\ln 10} \alpha z \end{aligned} \tag{2.84}$$

From Fig-2.25, the propagation distance z can be expressed as

$$z = R\phi \tag{2.85}$$

For 90^0 arc bent waveguide, above equation can be written as

$$z = \frac{\pi \times 90^0}{180^0} R = 1.57R \tag{2.86}$$

Substituting z in equation (2.84), we obtain the following expression for the bend

loss in a 90^0 arc waveguide-

$$T_B(90) = \frac{10}{\ln 10}\alpha \times 1.57R = 4.343\alpha \times 1.57R \tag{2.87}$$

S-bending loss

S-bends are one of the fundamental components in integrated optic devices. S-bends are used in the transition region in a number of devices such TMI coupler and Mach Zehnder (MZ) devices. Fig-2.26 shows the schematic view of two S-bends used in the transition region with bending radius R, bending height H_T, bending angle ϕ, transition length L_T and arc length S. From Fig-2.26, the

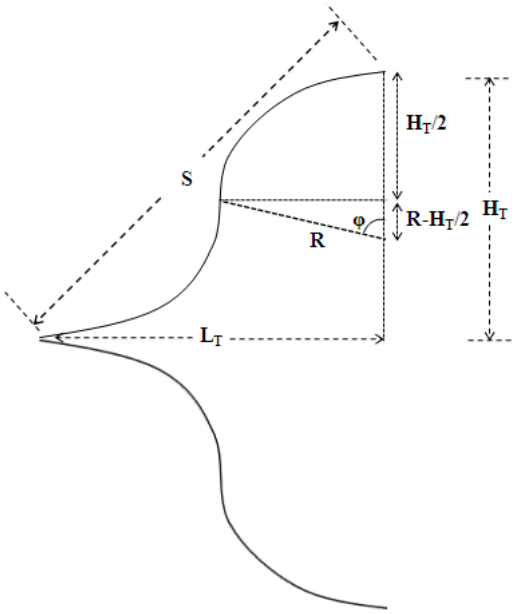

Figure 2.26: Schematic view of two S-bend used as transition waveguides

S-bend arc length can be expressed as

$$S = 2R\phi \tag{2.88}$$

From the geometry of Fig-2.26, the bending angle ϕ can be written as

$$\phi = \cos^{-1}\left(\frac{R - H_T/2}{R}\right) = \cos^{-1}\left(1 - \frac{H_T}{2R}\right) \tag{2.89}$$

Thus, equation (2.88) can be written as

$$S = 2R\cos^{-1}\left(1 - \frac{H_T}{2R}\right) \tag{2.90}$$

The S-bending loss in dB can be expressed as

$$\begin{aligned} T_S &= -\frac{10}{\ln 10}\ln\{\exp(-\alpha S)\} \\ &= \frac{10}{\ln 10}\alpha S \\ &= 4.343\alpha S \end{aligned} \tag{2.91}$$

Substituting S from equation (2.90), the expression (2.91) for S-bending loss is obtained as

$$\begin{aligned} T_S &= 4.343\alpha \times 2R\cos^{-1}\left(1-\frac{H_T}{2R}\right) \\ &= 8.686\alpha R\cos^{-1}\left(1-\frac{H_T}{2R}\right) \end{aligned} \tag{2.92}$$

2.4.5 KCl:Tl^0(1) color center lasers

Color centers refer to electrons (or holes) trapped by defects in insulating crystals [107]. Color centers are used in optically pumped lasers which are widely tunable over a number of wavelength bands such as ultraviolet, visible and infrared. Color centers are most easily created in the alkali halides. The phenomenon of laser action in color centers was first reported by Fritz and Menke [108] in 1965. Almost 10 years later, after the pioneering work by Fritz and Menke, Mollenauer and Olson [109] started the field of tunable color center lasers.

The presence of Tl(1) center was first discovered in 1980 [110]. The discovery of laser-active centers in KCl:Tl was made in 1981 [111] by W. Gellermann *et al.* The phenomenon was first attributed to Tl-F$_A$ center until 1983, when the L. F. Mollenauer *et al.* [112] and F. J. Ahlers [113] independently identified the new laser-active center as the Tl^0(1) center.

Although the Tl(1) center is observed in several alkali halides, only the center in KCl alkali hallide has gained practical interest due to several reasons such as small potential loss and stability [107]. The KCl:Tl^0(1) center does not show any detectable fading during laser action and thus, leads to the possibility of a given crystal to last indefinitely.

The stability may be attributed to the coulomb binding between the Tl atom (with negative charge) and the vacancy (with positive effective charge) [107]. The Tl(1) center in KCl may have a very long life time if stored at just a

little below room temperature. This exceptional stability as well as the special tuning range are the main reasons which have made the KCl:$Tl^0(1)$ center a most practical and important laser center, despite its lower efficiency [107].

Energy and pulse width of laser

The pulse width of a laser pulse is given by the full width at half maximum of the pulse, defined as the pulse duration at half maximum power of pulse. Schematic

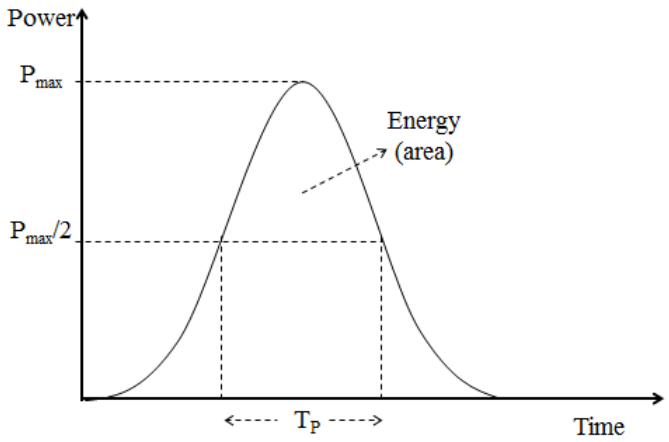

Figure 2.27: A laser pulse with peak power P_{max} and width T_P

view of a laser pulse with peak power P_{max} and pulse width T_P is shown in Fig-2.27. In the figure, the pulse width T_P is given by the duration of time at which the power of pulse becomes half of the peak power ($= P_{max}/2$). The energy of the pulse is given by the area covered by the curve for the power and can be expressed as $E = P_{max}t$.

Ultra-short pulse generation by mode locking

Laser pulses with short duration can be generated by using a wide variety of lasers having wavelengths in the ultraviolet, visible and infrared bands. Mode-locking is a technique used to generate laser pulses of extremely short duration. The basic concepts of mode locking for generation of ultra-short laser pulses are discussed in the following:

A mode locked laser usually consists of a pair of mirrors with the gain medium and other laser components enclosed in between them, as shown in Fig-2.28. For a distance of separation L_M between the two mirrors, the cavity round

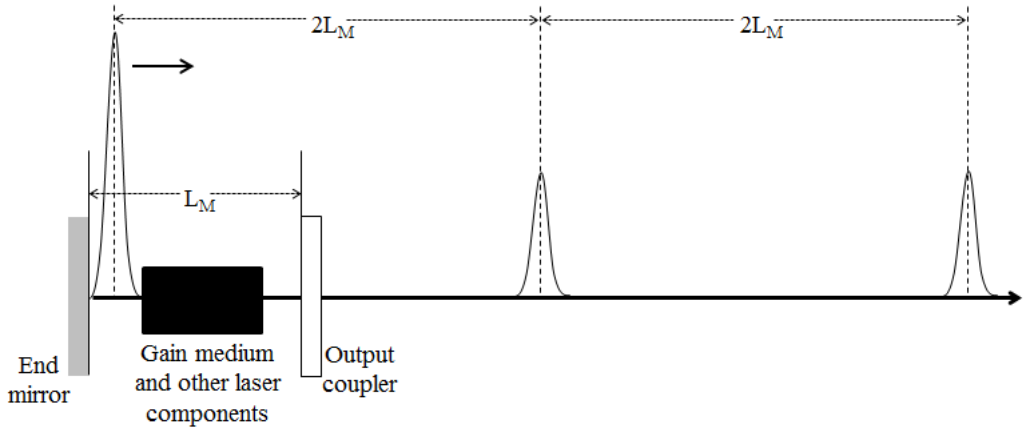

Figure 2.28: Schematic view of ultrashort laser pulse generation by mode-locking

trip time is given by [114]

$$T_R = \frac{2L_M}{c} \tag{2.93}$$

where, c is the velocity of light. For simplicity, the refractive index of the medium is taken as unity. In case of a continuous-wave (CW) laser or pulsed laser with a pulse duration greater than T_R, the radiation energy is spread out uniformly between the mirrors and confined into a small spatial region in the cavity. This single laser pulse confined between the mirrors bounces back and forth at the velocity of light. The output beam with ultra-short pulses arises from partial transmission of the confined laser pulse through the output coupler, as shown in Fig-2.28. Thus, the output beam consists of a train of pulses which are replica of the cavity pulse, separated by spatial distance $2L_M$ or by time T_R. The following are some properties of laser pulses generated by mode locking [114]

- The period of the train of pulses generated by mode locking is given by the cavity round trip time T_R.
- The peak power of the pulses increase quadratically as the number N of oscillating modes increases.
- The pulse width or full width at half maximum of pulse T_P decreases as the number N of oscillating modes increase ($T_P = T_R/N$).

2.5 Motivation

From the survey of previous works, it is clear that the following issues may be resolved for integrated optical processor components:

(a) Use of simple structure in fundamental all-optical logic gate components and optical power splitter for easy fabrication requiring less number of fabrication steps and high fabrication tolerance.

(b) Design of compact component for large scale integration of integrated optical processor.

(c) High speed tuning of optical power splitter in integrated optical processor.

To solve the above issues, we have proposed a surface plasmonic two-mode interference (SPTMI) waveguide coupler as a basic component for integrated optical processor device components. The issue relating to large and complicated size of the previously reported devices is solved by the simple and compact structure of the basic SPTMI device provided by the surface plasmonic waveguide based on TMI principle. Moreover, the optical pulse controlled operation of the basic device ensures a high operating speed of the optical processor components designed by using the basic structure.

2.6 Conclusion

In this chapter, we have presented a brief overview on the theoretical background and comprehensive literature required to achieve the objectives set in the thesis. From a comparative study among directional coupler, TMI coupler and MMI coupler, it is found that, the TMI coupler provides the most compact structure among the three types of planar waveguide couplers. We have also presented a review on the existing works on all-optical logic gates and tunable optical power splitter. With a knowledge of the theoretical concepts and previous literature discussed in this chapter, the research contributions are presented in the succeeding chapters.